
The School of Engineering of Tokai University publishes two kinds of Reports: the report written in English (once a year) and the one written in Japanese (once a year). The report written in English includes original papers, as well as the abstracts of the papers which appeared in the reports written in Japanese.

* * *

Any requests for this proceedings should be addressed to the Editorial Committee of Procceedings of the School of Engineering Tokai University, 4-1-1, Kitakaname, Hiratsuka-shi, Kanagawa-ken. Japan

September 30, 2021

Attention:
The name of this PROCEEDINGS has been changed from 2002 edition as follows.
「PROCEEDINGS OF *THE SCHOOL OF ENGINEERINGS* /
THE SCHOOL OF INFORMATION SCIENCE
AND TECHNOLOGY OF TOKAI UNIVERSITY」

C O N T E N T S

SCHOOL OF ENGINEERING

Technical Papers

Proc. Schl. Eng. Tokai Univ., Ser. E
46 (2021) 1-6
DOI: 10.18995/24343641.46.1

Characterization of the Membrane Topology and Physical Interaction of Human *N*-acetylglucosamine-1-phosphate Transferase

by

Tetsuo TAKAHASHI[*1], Kazuhiro NISHIMURA[*2], Naohiko MAEDA[*3] and Riki OSHIRO[*2]

(Received on Mar. 31, 2021 and accepted on May 25, 2021)

Abstract

Human *N*-acetylglucosamine-1-phosphate (GlcNAc-1-P) transferase (hGPT) is localized on the rough endoplasmic reticulum (rER) membrane as a multispan transmembrane protein and involved in the first step of assembly of dolichol-linked oligosaccharides (DLOs) which are precursors of *N*-glycan. In this study, we analyzed the membrane topology of hGPT using the yeast split-ubiquitin system (YSUS). The obtained data demonstrated that hGPT includes eight transmembrane domains (TMDs) and shows characteristics of the type IV membrane topology, where both *N*- and *C*-termini are orientated toward the cytosolic side of the rER membrane. Using the YSUS, we also demonstrated that hGPT physically interacts with hAlg13, which is the cytosolic subunit of human β-1,4 GlcNAc transferase (hNAGT), hDPM2 and hDPM3 transmembrane subunits of human dolichol-phosphate-mannose (DPM) synthase (hDPMS), human dolichol kinase (hDK) and human dolichol pyrophosphate phosphatase (hDPP). These results strongly suggest that hGPT cooperates with other dolichol-phosphate (Dol-P)-utilizing enzymes in the biosynthetic pathway of DLO.

Keywords: hGPT, Dolichol-linked oligosaccharide, Split-ubiquitin system, Membrane topology, Physical interaction

1. Introduction

N-glycosylation is one of the critical events for the maintenance of both structure and function of many glycoproteins in higher eukaryotes. The *N*-glycans on glycoproteins are primarily derived from the dolichol-linked oligosaccharides (DLOs), which are biosynthesized on the rough endoplasmic reticulum (rER) membrane[1)]. As shown in Fig. 1, the assembly process of DLOs is further divided into three stages: first, early assembly of up to $Man_5GlcNAc_2$-PP-Dolichol (Dol) on the cytoplasmic side by UDP-GlcNAc or GDP-Man dependent glycosyltransferases; second, translocation of $Man_5GlcNAc_2$-PP-Dol into the luminal side by a putative flippase; and finally, late assembly of full-sized DLO ($Glc_3Man_9GlcNAc_2$-PP-Dol) by Dol-P-Man or Dol-P-Glc dependent glycosyltransferases[2-5)]. These highly ordered steps are well conserved all through eukaryotes.

The *N*-acetylglucosamine-1-phosphate (GlcNAc-1-P) transferase (GPT) is involved in the first step of DLO assembly. Namely, this enzyme catalyzes the transfer reaction of GlcNAc-1-P from UDP-GlcNAc to dolichol phosphate (Dol-P), forming GlcNAc-PP-Dol in the cytoplasmic side of

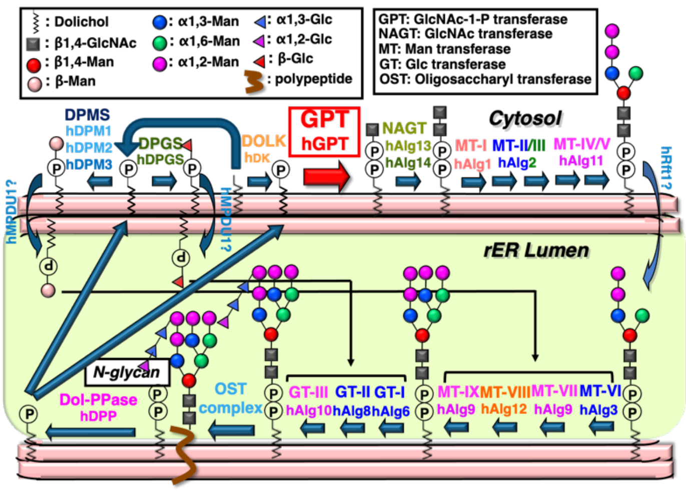

Fig. 1 Assembly of dolichol-linked oligosaccharides (DLOs) and site of action regarding human *N*-acetylglucosamine-1-phosphate transferase (hGPT).

the rER membrane (red arrow in Fig. 1). The gene encoding the GPT were originally identified as a tunicamycin-resistant gene[6)], and isolated firstly in budding yeast as the *ALG7* gene[7)], and secondly in hamster[8)] and mouse[9)]. Thereafter, human *GPT* (*hGPT*) gene orthologous to hamster *GPT* gene has been cloned by complementation of yeast *alg7* mutations[10)]. Although the membrane topology of hamster GPT has been biochemically characterized, that of hGPT remained to be

*1 Associate Professor, Department of Applied Biochemistry
*2 Undergraduate Student, Department of Applied Biochemistry
*3 Graduate Student, Course of Industrial Chemistry

Table I The PCR primers used in this study. Additional sequences containing a *Sfi* I- cleavage site are shown in lowercase letters.

Primer name	Nucleotide sequence	Purpose
GBP_fw	5'-tgtaatggccattacggccATGTGGGCCTTCTCGGAATTG-3'	PCR cloning of *hGPT* into pBT-N, pBT-STE and pPR-N
GBP_rv	5'-gcctttggccgaggcggccCAGACATCATAGAAGAGTCGAACG-3'	PCR cloning of *hGPT* into pBT-N, pBT-STE, pPR-N and pPR-STE
GPST_fw	5'-gtcagtggccattacggcccgATGTGGGCCTTCTCGGAATTG-3'	PCR cloning of *hGPT* into pPR-STE
G(LR2)BP_rv	5'-gcctttggccgaggcggccCTGGGATTCTGGGATCTGCTG-3'	PCR cloning of *hGPT* from *N*-terminus to LR2 into pBT-C
G(LR3)BP_rv	5'-gcctttggccgaggcggccTCATGGTGGGGAATGCCTTAC-3'	PCR cloning of *hGPT* from *N*-terminus to LR3 into pBT-C
G(LR4)BP_rv	5'-gcctttggccgaggcggccCTTATGGCGCCAGCGCAG-3'	PCR cloning of *hGPT* from *N*-terminus to LR4 into pBT-C
G(LR5)BP_rv	5'-gcctttggccgaggcggccCCCAAGTCCAGATGCAGGC-3'	PCR cloning of *hGPT* from *N*-terminus to LR5 into pBT-C
G(LR6)BP_rv	5'-gcctttggccgaggcggccCTGGCCAGCCTCTAGGCCG-3'	PCR cloning of *hGPT* from *N*-terminus to LR6 into pBT-C
G(LR7)BP_rv	5'-gcctttggccgaggcggccACATGATCATCCCGACAATCAC-3'	PCR cloning of *hGPT* from *N*-terminus to LR7 into pBT-C
G(LR8)BP_rv	5'-gcctttggccgaggcggccCCCACAAACACCCGTGATGG-3'	PCR cloning of *hGPT* from *N*-terminus to LR8 into pBT-C
G(LR9)BP_rv	5'-gcctttggccgaggcggccCATGGTCTTGCTGAAGTGTCC-3'	PCR cloning of *hGPT* from *N*-terminus to LR9 into pBT-C

experimentally analyzed in detail. Therefore, in this study, we first investigated the membrane topology of hGPT using the yeast split-ubiquitin system (YSUS)[11-14], a yeast two-hybrid system that can specifically detect the physical interaction between two membrane proteins[15-18]. In addition, we also characterized the physical interactions of hGPT with other enzymes involved in the DLO assembly using the YSUS.

2. Experimental Methods

2.1 *Prediction of the membrane topology of hGPT*

In order to predict the membrane topology of hGPT protein, two WWW algorithms servers, TMHMM version 2[19] (https://www.cbs.dtu.dk/services/TMHMM) and TOPCONS[20] (https://topcons.cbr.su.se) were used. On each WEB site, the amino acid sequence of hGPT protein composed of 408 residues was registered and surveyed regarding transmembrane domain (TMD) and membrane topology.

2.2 *Construction of recombinant plasmids for the YSUS*

The coding region of *hGPT* gene was amplified from the human cDNA pools derived from the human brain by standard PCR method[21] using specific primers listed in Table 1. It was then digested with *Sfi* I, purified and ligated to the pBT-N or pBT-STE plasmid vector for expression of hGPT bait protein which has *N*- or *C*-terminal tag (Cub) prepared in the YSUS, respectively. Preparation of each recombinant plasmid was conducted by standard cloning method[22] with *Escherichia coli* JM109 strain. The constructs for expression of hGPT prey protein were also prepared by the same procedure, except usage of the pPR-N and pPR-STE plasmid vectors instead of pBT-N and pBT-STE.

In order to analyze the membrane topology of hGPT, nine pBT-C vector-based constructs for expression of truncated versions of hGPT bait in yeast cell (pBT-C-hGPT LR2 to pBT-C-hGPT LR10) were prepared via PCR cloning described above.

In order to analyze the physical interactions of hGPT with thirteen other enzymes involved in DLO assembly (shown in Fig. 1), the prey constructs[23] for their expression were also prepared via PCR cloning described above.

2.3 *Assays for the membrane topology of hGPT*

The bait constructs, pBT-N-hGPT, pBT-STE-hGPT and nine pBT-C-hGPT LR series were used for co-transformation of *Saccharomyces cerevisiae* NMY51 strain, together with the positive or negative control prey construct, pAI-Alg5 or pDL-Alg5. The transformation of yeast cells was carried out by the standard method[24]. The co-transformants obtained on the synthetic dextrose (SD) medium lacking leucine and tryptophan (SD-LW) were then subject to the growth examination on the SD medium lacking leucine, tryptophan and histidine (SD-LWH) and SD medium lacking leucine, tryptophan, histidine and adenine (SD-LWHA) according to the manual supplied by Dualsystems Biotech (www.dualsystems.com).

2.4 *Assays for the physical interaction of hGPT*

The bait construct, pBT-N-hGPT or pBT-STE-hGPT was combined with any prey construct of thirteen enzymes involved in DLO assembly (shown in Fig. 1), and then they were used for co-transformation of the yeast NMY51 strain. After the co-transformation, the resultant co-transformants on SD-LW medium were subject to growth examination with SD-LWH and SD-LWHA media, according to the same procedure as described above.

3. Results and Discussion

3.1 *The membrane topology of hGPT*

hGPT protein is made up with 408 amino acid residues. First, we started from predicting the membrane topology of

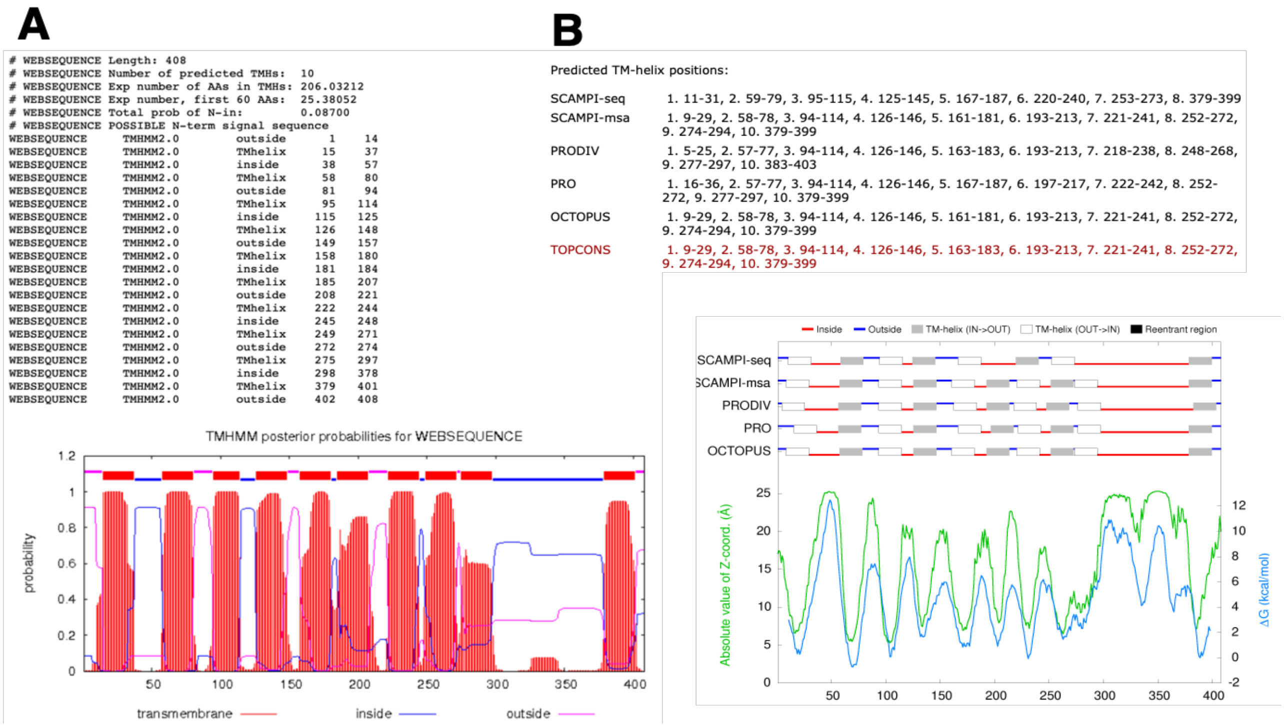

Fig. 2 Prediction of the membrane topology of hGPT protein using TMHMM (A) and TOPCONS (B) algorithms. The horizontal bars and boxes in the two graphs indicates predicted eleven loop regions (LRs 1 to 11) and ten hydrophobic regions (HRs 1 to 10) of hGPT protein, respectively.

hGPT protein with two algorithms, TMHMM server and TOPCONS, freely available on WEB sites. Both algorithm programs predicted eleven loop regions (LRs 1 to 11) and ten hydrophobic regions (HRs 1 to 10) corresponding to TMDs in hGPT protein (Fig. 2). Moreover, the two programs also predicted that both the *N*- and *C*-termini of hGPT would be orientated toward cytoplasm of the rER membrane (Fig. 2). These predictions were well incident with the previous membrane topological model regarding hamster GPT protein obtained by biochemical analysis[25].

In order to confirm the predictions, we applied the YSUS to our analysis. The negative and positive control prey constructs (pDL-Alg5 and pAI-Alg5, respectively) prepared in the YSUS are designed to express Nub tag terminally fused to the Alg5 protein in cytoplasmic side of the rER, and readily available to ascertain whether the terminal Cub tag of the bait protein expressed in the rER membrane is located in the cytoplasm or lumen[26, 27]. Therefore, we prepared two bait constructs, pBT-N-hGPT and pBT-STE-hGPT, which express a full-length hGPT protein with *N*- and *C*-terminal Cub tags, respectively. We also prepared nine bait constructs, pBT-C-hGPT/LR2 to pBT-C-hGPT/LR10, each of which expresses a truncated version of hGPT, whose *C*-terminal Cub tag is respectively fused to LR2 to LR10 of hGPT. Each bait construct was combined with the pDL-Alg5 or pAI-Alg5 control prey, and then they were used for co-transformation of yeast NMY51 cells. The resultant co-transformants grown on SD-LW plates were subsequently subject to examination of growth on SD-LWH and SD-LWHA selective media.

In growth examination, co-transformants of the pBT-N-hGPT or pBT-STE-hGPT bait with the pAI-Alg5 positive control prey have well grown on both SD-LWH and SD-LWHA plates (top and bottom red frames in Fig. 3). On the contrary, those of with the pDL-Alg5 negative control prey exhibited no growth on both media (Fig. 3), indicating that the terminal Cub tag fused to bait protein specifically interacted with Nub tag of pAI-Alg5 located in the cytoplasm. From these results, it was concluded that both *N*- and *C*-termini of hGPT should be located in the cytoplasmic side of the rER membrane.

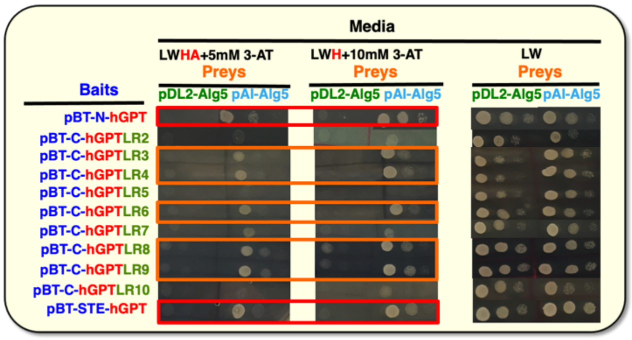

Fig. 3 Growth examination of co-transformants with hGPT bait / control prey constructs. After the selection of colonies derived from the co-transformants on the SD-LW medium, their suspensions were diluted with sterilized water and adjusted to the OD_{600} values of 1.0, 0.1 and 0.01 (from left to right). These diluents were orderly spotted on the SD-LWH and SD-LWHA media which contain 3-amino-1, 2, 4-triazole (3-AT) for reporter detection, and SD-LW media for growth control, and then incubated at 30 ºC for 2~4 days.

Of the co-transformants of nine bait constructs expressing truncated hGPT with the pAI-Alg5, those of the pBT-C-hGPT/LR3, pBT-C-hGPT/LR4, pBT-C-hGPT/LR6, pBT-C-hGPT/LR8 and pBT-C-hGPT/LR9 displayed growth activities

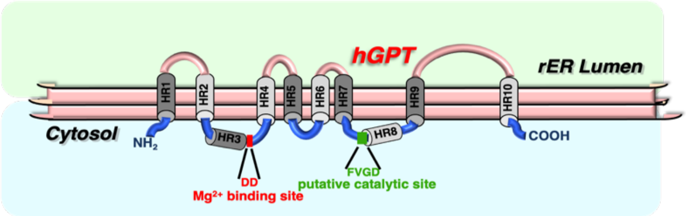

Fig. 4 The putative model of the membrane topology of hGPT speculated by the YSUS analyses in this study.

(orange frames in Fig. 3), while those of the pBT-C-hGPT/LR2, pBT-C-hGPT/LR5, pBT-C-hGPT/LR7 and pBT-C-hGPT/LR10 did not (Fig. 3).

Taken together, these observations demonstrated that *N*-terminus (or LR1), five internal loop regions (LR3, LR4, LR6, LR8 and LR9) and *C*-terminus (or LR11) of hGPT are located in the cytoplasm and that four remaining internal loop regions (LR2, LR5, LR7 and LR10) are located within the rER lumen (Fig. 4). This model of the membrane topology of hGPT is different from both model of hamster GPT previously proposed[25] and our prediction represented in Fig. 2, in that hGPT has eight TMDs with two hydrophobic regions, HR3 and HR8, resident in the cytoplasm (Fig. 4). As shown in Fig. 4, hGPT possesses a DDxx motif, which might bind the co-factor Mg^{2+} ion, and a putative catalytic motif FVDG. These should be located in the cytoplasmic side of the rER membrane, because the sugar nucleotide UDP-GlcNAc, the donor substrate of hGPT, exists only in the cytosol and the transfer reaction of GlcNAc-1-P from UDP-GlcNAc to Dol-P also occurs in the same side. Therefore, our model represented in Fig. 4 are well compatible with the positional restriction of these motifs, although it remains to be possible that the HR3 and HR8 are potential membrane-embedded domains.

3.2 *The physical interaction of hGPT*

In order to test whether hGPT physically interacts with other enzymes in the same DLO assembly pathway, the bait construct pBT-N-hGPT or pBT-STE-hGPT was combined with each prey construct of various enzymes which participate in DLO assembly, and the co-transformations of NMY51 cells were conducted. The results of growth examination of co-transformants were shown in Figs. 5 and 6.

First, we investigated the physical interaction of hGPT with various glycosyltransferases involved in the early (panel A of Fig. 5) and late (panel B of Fig. 5) assembly of DLO. As seen in Fig. 1, hGPT, human GlcNAc transferase (hNAGT) and three human GDP-Man-dependent mannosyltransferases (hAlg1, hAlg2 and hAlg11) are responsible for the early assembly, while three human Dol-P-Man-dependent mannosyltransferases (hAlg3, hAlg9 and hAlg12) and three human Dol-P-Glc-dependent glucosyltransferases (hAlg6, hAlg8 and hAlg10) are related in the late assembly.

In the case of the pBT-N-hGPT bait, all co-transformants with any prey tested did not grow on the SD-LWH and SD-LWHA selective media (blue frames in the panel A and B of Fig. 5). However, in the case of the pBT-STE-hGPT bait, co-transformants with the pPR-N-hGPT prey displayed strong growth (red frame in the panel A of Fig. 5). This result suggests that hGPT might form a homo-dimeric complex on the rER membrane. As hamster GPT has been demonstrated to

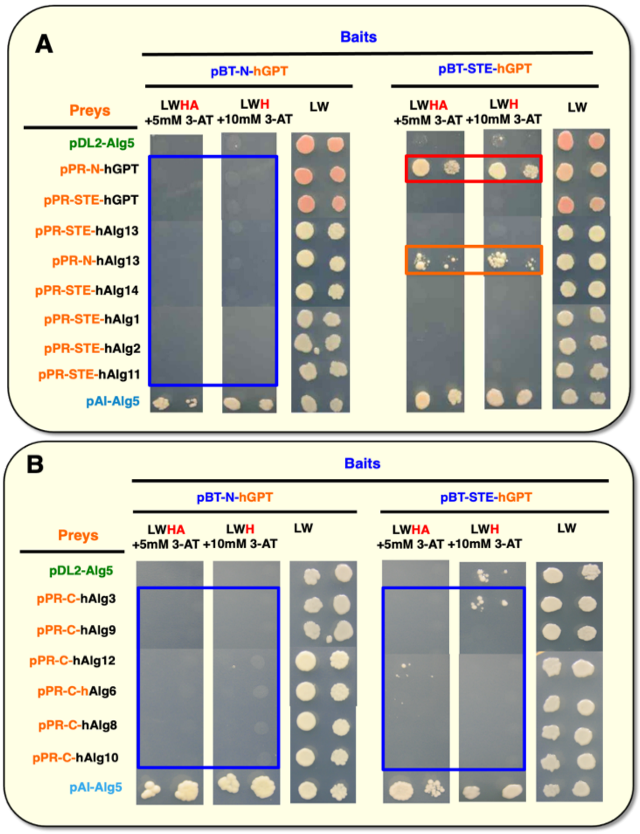

Fig. 5 Growth examination of co-transformants of hGPT bait with preys of various glycosyltransferases involved in early (panel A) and late (panel B) assembly of DLO. The experiments were performed according to the same procedure as described in the legend of Fig. 3, except that the spotting of diluents of OD$_{600}$ values 0.01 was omitted.

be homo-oligomerized by the biochemical analysis with chemical cross-linker[28], our result of the hGPT-to-hGPT interaction was coincident with that of hamster GPT oligomerization.

Moreover, co-transformants with the pPR-N-hAlg13 prey displayed weak growth (orange frame in the panel A of Fig. 5). As hAlg13 is a cytosolic catalytic subunit of hNAGT and known to physically interacts with hAlg14, a transmembrane subunit of hNAGT, it is speculated that hGPT might weakly contact with hNAGT via hAlg13. This possibility that hGPT would physically interact with hNAGT is supported by our unpublished observation that the co-transformants of the pBT-STE-hAlg14 bait with the pPR-N-hGPT prey were able to grow on both selective media, and the report that yeast Alg7p (corresponding to yeast GPT) physically interacts with yeast Alg13p and Alg14p[29].

Next, we examined the physical interaction of hGPT with enzymes which supply the donor substrate (Dol-P-Man and Dol-P-Glc) and the acceptor substrate (Dol-P) to the DLO-related glycosyltransferase described above. As shown in Fig. 6, co-transformants of hGPT with hDPM2 or hDPM3 were able to well grow on the LWH and LWHA media (upper red frames in the Fig. 6). They are subunits of the hDPMS, which utilizes the Dol-P as acceptor substrate as well as hGPT. Hence, GPT and hDPMS could tightly contact with each other. Against hDPGS, another utilizer of Dol-P, hGPT also might contact, because the co-transformants of the pBT-STE-hGPT

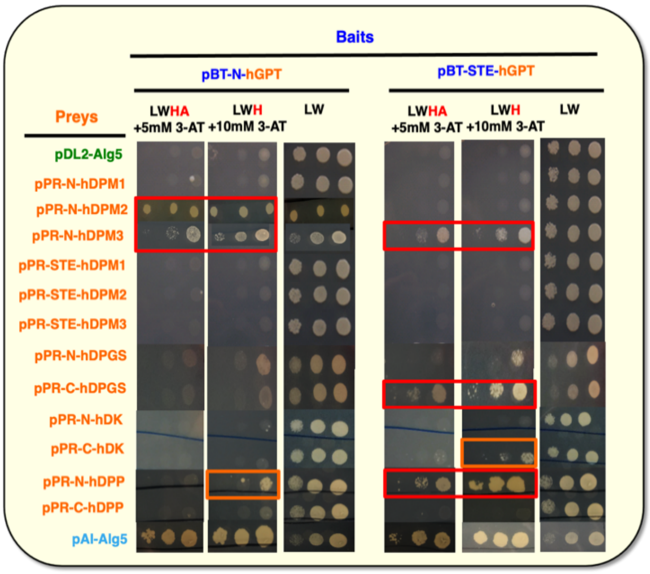

Fig. 6 Growth examination of co-transformants of hGPT bait with preys of enzymes which directly supply substrates (Dol-P, Dol-P-Man and Dol-P-Glc) to glycosyltransferases biosynthesizing DLO. The experiments were performed according to the same procedure as described in the legend of Fig. 3.

bait with the pPR-C-hDPGS prey were able to grow on selective media (right middle red frame in Fig. 6).

Two human enzymes, hDK and hDPP, are responsible for producing *de novo* and re-producing Dol-P, respectively (Fig. 1). We obtained results that co-transformants of the pBT-STE-hGPT bait with the pPR-C-hDK prey exhibited relatively weak viability on selective media, as well as those of the pBT-N-hGPT with the pPR-N-hDPP (orange frames in Fig. 6). In addition, we also obtained another result that the co-transformants of the pBT-STE-hGPT bait with the pPR-N-hDPP prey displayed stable viability on the media (right lower red frame in Fig. 6). Considering together, these observations suggests that hGPT might preferentially consider hDPP rather than hDK, as supplier of Dol-P.

5. Conclusion

In order to determine the membrane topology of hGPT involved in the first step of early assembly of DLO, the YSUS was utilized. Growth tests on the YSUS demonstrated that hGPT protein contains at least eight TMDs, with its *N*- and *C*-termini located in the cytoplasm.

Regarding the physical interactions of hGPT, we obtained several novel informations via analyses by the YSUS ; First, hGPT might homo-dimerize on the rER membrane. Second, hGPT might specifically contact with several other enzymes in DLO biosynthetic pathway, such as hNAGT, hDPMS, hDPGS, hDK and hDPP. Third, the degree of physical interactions of hGPT with several enzymes are obviously different from each other.

The physical interaction between two membrane enzymes could play a role in positively or negatively altering their enzymatic activities. Taking the fact that hGPT first serves the DLO assembly into consideration, the observations in this study suggest that it might be one of critical enzymes for regulating the yield of DLOs, followed by *N*-glycans on the glycoprotein in eukaryotic cells. In order to establish the importance of this enzyme in regulation of DLO assembly pathway, further analyses are necessary to be carried out.

References

1) M. Aebi: *N*-linked protein glycosylation in the ER, Biochim. Biophys. Acta, Vol. 1833, pp. 2430-2437 (2013).
2) A. D. Elbein: Inhibitors of the biosynthesis and processing of *N*-linked oligosaccharides, CRC Crit. Rev. Biochem., Vol.16, pp. 21-49 (1984).
3) A. Herscovics and P. Orlean: Glycoprotein biosynthesis in yeast, FASEB J., Vol. **7,** pp. 540-550 (1993).
4) M. A. Kukuruzinska, M. L. E. Bergh and B. J. Jackson: Protein glycosylation in yeast, Ann. Rev. Biochem., Vol. 56, pp. 915-944 (1987).
5) C. B. Hirschberg and M. D. Snider: Topography of glycosylation in the rough endoplasmic reticulum and Golgi apparatus, Annu. Rev. Biochem., Vol. 56, pp. 63-87 (1987).
6) J. Rine, W. Hansen, E. Hardeman and R. W. Davis: Targeted selection of recombinant clones through gene dosage effects, Proc. Natl. Acad. Sci. USA, Vol. 80, pp. 6750-6754 (1983).
7) G. Barnes, W. J. Hansen, C. L. Holcomb and J. Rine: Asparagine-linked glycosylation in *Saccharomyces cerevisiae*: genetic analysis of an early step, Mol. Cell Biol., Vol. 4, No. 11, pp. 2381-2388 (1984).
8) J. R. Scocca and S. S. Krag: Sequence of a cDNA that specifies the uridine diphosphate *N*-acetyl-D-glucosamine: dolichol phosphate *N*-acetylglucosamine-1-phosphate transferase from Chinese hamster ovary cells, J. Biol. Chem., Vol. 265, pp. 20621-26026 (1990).
9) B. Rajput, M. A. Jie, N. Muniappa, L. Schantz, S. L. Naylor, P. A. Lalley and I. K. Vijay: Mouse UDP-GlcNAc: dolichyl-phosphate *N*-acetyl-glucosamine-phosphotransferase: molecular cloning of the cDNA, generation of anti-peptide antibodies and chromosomal localization, Biochem. J., Vol. 285, pp. 985-992 (1992).
10) V. Eckert, M. Blank, R. Mazhari-Tabrizi, D. Mumberg, M. Funk and R. T. Schwarz: Cloning and functional expression of the human GlcNAc-1-P transferase, the enzyme for the committed step of the dolichol cycle, by heterologous complementation in *Saccharomyces cerevisiae*, Glycobiology, Vol. 8, pp. 77-85 (1998).
11) N. Johnsson and A. Varshavsky: Split ubiquitin as a sensor of protein interactions *in vivo*, Proc. Natl. Acad. Sci. USA, Vol. 91, No. 22, pp. 10340-10344 (1994).
12) I. Stagljar, C. Korostensky, N. Johnsson and S. te Heesen: A genetic system based on split-ubiquitin for the analysis of interactions between membrane proteins *in vivo*, Proc. Natl. Acad. Sci. USA, Vol. 95, No. 9, pp. 5187-5192 (1998).
13) M. Fetchko and I. Stagljar: Application of the split-ubiquitin membrane yeast two-hybrid system to investigate membrane protein interactions, Methods, Vol. 32, pp. 349-362 (2004).

14) S. Thaminy, J. Miller and I. Stagljar: The split-ubiquitin membrane-based yeast two-hybrid system, Methods. Mol. Biol., Vol. 261, pp. 297-312 (2004).
15) M. Dünnwald, A. Varshavsky and N. Johnsson: Detection of transient *in vivo* interaction between substrate and transporter during protein translocation into the endoplasmic reticulum, Mol. Biol. Cell, Vol. 10, pp. 329-344 (1999).
16) M. J. Massaad and A. Herscovics: Interaction of the endoplasmic reticulum alpha 1,2-mannosidase Mns1p with Rer1p using the split-ubiquitin system, J. Cell Sci., Vol. 114, pp. 4629-4635 (2001).
17) W. Scheper, S. Thaminy, S. Kais, I. Stagljar and K. Römisch: Coordination of *N*-glycosylation and protein translocation across the endoplasmic reticulum membrane by Sss1 protein, J. Biol. Chem., Vol. 278, No. 39, pp. 37998-38003 (2003).
18) A. Yan and W. J. Lennarz: Studies on yeast oligosaccharyl transferase subunits using the split-ubiquitin system: Topological features and *in vivo* interactions, Proc. Natl. Acad. Sci. USA, Vol. 102, No. 20, pp. 7121-7126 (2005).
19) A. Krogh, B. Larsson, G. von Heijne and E. L. Sonnhammer: Predicting transmembrane protein topology with a hidden Markov model: application to complete genomes, J. Mol. Biol., Vol. 305, No. 3, pp. 567-580 (2001).
20) K. D. Tsirigos, C. Peters, N. Shu, L. Käll and A. Elofsson: The TOPCONS web server for consensus prediction of membrane protein topology and signal peptides, Nucleic Acids Res., 43 (Web Server issue) W401-407 (2005).
21) H. A. Erlich: *PCR Technology*, Stockton Press, pp.61-70 (1989).
22) L. Sambrook, E. F. Fritsch and T. Maniatis: *Molecular Cloning: A Laboratory Manual*, Second edition, Cold Spring Harbor Laboratory Press, New York (1989).
23) T. Takahashi and X.-D. Gao: Physical interactions among human glycosyltarnsferases involved in dolichol-linked oligosaccharide biosynthesis, Trends in Glycoscience and Glycotechnology, Vol. 24, pp. 65-77 (2012).
24) H. Ito, Y. Fukuda, K. Murata and A. Kimura: Transformation of intact yeast cells treated with alkali cations, J. Bacteriol., Vol. 153, No. 1, pp. 163-168 (1983).
25) N. Dan, R. B. Middleton and M. A. Lehrman: Hamster UDP-*N*-acetylglucosamine: dolichol-P *N*-acetylglucosamine-1-P transferase has multiple transmembrane spans and a critical cytosolic loop, J. Biol. Chem., Vol. 271, No. 48, pp. 30717-30724 (1996).
26) T. Takahashi, N. Yamada and N. Kurimoto: Analyses on the physical interactions of the human dolichyl-phosphate mannose synthase, Proc. Schl. Eng. Tokai Univ., Ser. J., Vol. 57, No. 1, pp. 5-10 (2017).
27) T. Takahashi and T. Takeuchi: Membrane topological characterization of the human Alg14 protein, Proc. Schl. Eng. Tokai Univ., Ser. E., Vol. 44, pp. 1-6 (2019).
28) N. Dan and M. A. Lehrman: Oligomerization of hamster UDP-GlcNAc: Dolichol-P GlcNAc-1-P transferase, an enzyme with multiple transmembrane spans, J. Biol. Chem., Vol. 272, No. 22, pp. 14214-14219 (1997).
29) C. Noffz, S. Keppler-Ross and N. Dean: Hetero-oligomeric interactions between early glycosyltransferases of the dolichol cycle, Glycobiology, Vol. 19, No. 5 pp. 472-478 (2009).

Proc. Schl. Eng. Tokai Univ., Ser. E
46 (2021) 7-13
DOI: 10.18995/24343641.46.7

Transmission Network Expansion Planning Using Nose Curve Index

by

Fortunatus Raymond KIHAKA[*1] and Masachika ISHIMARU[*2]

(Received on March 30, 2021 and accepted on May 25, 2021)

Abstract

Power systems are becoming more sensitive and complex due to the rapid increase in power demand. As a result, power systems experience voltage instability, line overloading and power system blackouts. In response, utility companies are forced to plan for short-term and long-term grid expansion to meet the system requirements. The optimal transmission expansion plan must be determined prior to implementation. However, it has always been difficult to find the optimal solution to the problem in an actual power system due to its large scale, complexity, and various uncertainties. Several techniques are used to solve the constrained transmission expansion planning problem. This paper focuses on the conventional approach and proposes a modified approach which considers the nose curve index as a constraint. The main objective of planning is to minimize investment costs needed for new network elements while meeting necessary operation constraints. A system power flow analysis is performed using the analytical software PSS®E, and the resulting nose curves are plotted using Microsoft Excel. The grid network of Tanzania is chosen as the reference power system.

Keywords: Transmission expansion, Voltage instability, Dynamic programming, Voltage profile, Nose curve index

1. Introduction

The voltage instability is one of the main causes of power system blackout. Most of the previous power system blackouts that happened worldwide were caused by voltage instability [1)]. Voltage instability can be defined as the failure of an electrical power system to sustain the voltage magnitudes at all buses remain the same after the electrical power system is being exposed to a disturbance [2-6)]. The grid networks are subjected to transmission expansion planning to meet the future power demand while satisfying the system reliability conditions at the least cost investment. The main purpose of transmission network expansion planning is to determine appropriate time, location, and capacity of transmission lines to be added to the power system [7)]. The transmission network expansion planning can be considered as static which focuses on planning for a single year or dynamic which focuses on several years [8)]. In practical, power system problems are often formulated with some constraints imposed on their variables [9).] Each planning constraints are to be satisfied to reach the optimal solution. The voltage profile is a critical constraint considered for short-term and long-term transmission expansion planning problem decision making.

In finding the optimal solution of the problem in a practical power system has always been a challenging issue due to its large dimension, complexity, and various uncertainties. There are several techniques used to solve the constrained transmission expansion planning problem. Dynamic Programming is one of the techniques used for multistage decision problems and originally was developed in 1950s by Bellman [7)]. It is a widely used technique in power system expansion planning studies. It is a multistage decision problem which can be decomposed into a sequence of single stage problems, the stages can be different times, different spaces, or different levels and solved successively [7)].

In this study the conventional transmission expansion planning approach is considered. The paper also proposes a new modified transmission expansion planning which considers the nose curve index (voltage sensitivity factor) as a key constraint to system expansion [6)]. The base case, conventional approach and proposed approach results will be compared. In testing the effectiveness of the proposed

[*1] Graduate Student, Course of Electrical and Electronic Engineering
[*2] Junior assistant Professor, Department of Electrical and Electronic Engineering

approach, the Tanzania grid network is used to plot the nose curves.

The nose curves are obtained by performing system power flow simulation. For every series of power flow, the load of the electrical power system is increased until the point where the system is noTable to operate any longer. The variation values of real power with the value of load are plotted as the nose curve [10]. The system load flow analysis is performed using PSS®E and the resulting nose curves are plotted using Microsoft Excel. The load flow study is normally performed during planning stage to test the results against the grid planning and operation criteria.

2. Transmission expansion planning problem

Transmission network expansion planning is an important part of power system planning with the objective of acquiring the most optimal plan for the network expansion. The transmission network expansion planning problem consists of finding new transmission lines which can be constructed to deliver power to load centers in efficient and reliable manner from the power nodes [8,11]. The added transmission lines increase the investment costs. The main objective of the transmission expansion is to minimize the total investment cost, maximize benefits subject to satisfying the technical constraints of the transmission network. The objective function is:

$$\text{minimize} \sum_{(i,j)}^{n} C_{ij}\, x_{ij} \qquad (1)$$

subject to

$$PG_{ref\_i} - PG_i = 0 \qquad (2)$$

$$PL_{ref\_i} - PL_i = 0 \qquad (3)$$

$$QL_{ref\_i} - QL_i = 0 \qquad (4)$$

$$0.98 \le V_i \le 1.02 \qquad (5)$$

where,

$$P_i = \sum_{j=1}^{N}\left[G(x_{ij})e_i e_j - B(x_{ij})e_i f_j + G(x_{ij})f_i f_j + B(x_{ij})f_i e_j\right]$$

$$Q_i = \sum_{j=1}^{N}\left[G(x_{ij})f_i e_j - B(x_{ij})f_i f_j - G(x_{ij})e_i f_j - B(x_{ij})e_i e_j\right]$$

i,j= Transmission line nodes
x_{ij} = Building parallel line from node i to node j
$G(x_{ij})$ and $B(x_{ij})$ are function of parameter x_{ij}
$V_i = e_i + jf_i$
V_i = Voltage at bus i
PG_i = Generated power at bus i
PL_i = Load real power at bus i
QL_i = Load ractive power at bus i

The objective function represents the investment cost. The constraint in equations 2,3 and 4 represents the conservation of power in each node. The constraints in equation 5 refers to voltage limits. The real and reactive power at each node is expressed in terms of bus voltage [12].

3. Voltage stability index by nose curve description

The nose curves indicate the relationship between voltage and active power of the system. This gives the available amount of active power margin before the point of voltage collapse. The voltage of the bus is monitored against the changes in real power consumption. As the load is increased voltage decreases and reaches a nose point, any further increase in load causes instability of the system [4,10]. When the active power is increased the voltage drops due to increase of load admittance. Hence, nose curve identifies the maximum load that can be supplied by the system and the resulting critical voltage.

Consider a simple system consisting of source with voltage Vs∠0 and load at voltage Vr∠δ fed by an infinite bus transmission system as shown in Fig. 1. The resistance of the transmission line connecting the source and the load is small and is neglected, real and reactive powers are given by the equations 6 and 7 [10,13].

$$P = V_r I \cos\theta = \frac{V_s V_r}{X}\sin\delta \qquad (6)$$

$$Q = V_r I \sin\theta = \frac{V_s V_r}{X}\cos\delta - \frac{V_r^{\,2}}{X} \qquad (7)$$

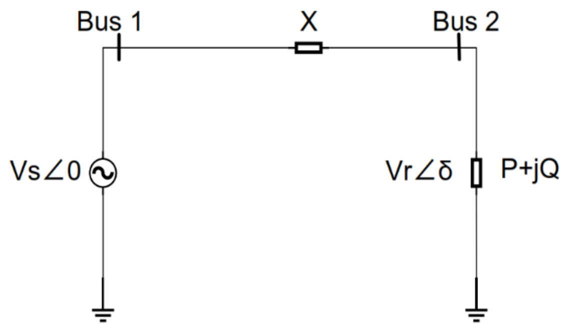

Fig. 1 Simple power system network.

Combining equation 6 and 7 using trigonometric identity $cos^2\delta + sin^2\delta = 1$ to eliminate the load angle [13].

$$\left(\frac{V_s V_r}{X}\right)^2 = P^2 + \left(Q + \frac{V_R^2}{X}\right)^2$$

$$P^2 = \left(\frac{V_s V_r}{X}\right)^2 - \left(Q + \frac{V_R^2}{X}\right)^2$$

$$P = \sqrt{\left(\frac{V_s V_r}{X}\right)^2 - \left(Q + \frac{V_R^2}{X}\right)^2}$$

Considering resistive load, then $Q = 0$ the equation can more be simplified.

$$P = \sqrt{\left(\frac{V_s V_r}{X}\right)^2 - \left(\frac{V_R^2}{X}\right)^2} \tag{8}$$

The relationship in equation 8 is the nose curve equation which relates various power system parameters. A plot of V against P is shown in Fig. 2 [14]. To each point P, there are two solutions for voltage, one is sTable solution, and the other one is unsTable solution [11]. In normal operation of any power system in stability region is limited to the upper part of the curve. In addition, normal loading margin P_{margin} between the maximum permissible demand and the nose is usually used as static voltage stability indicator [4,10,15]. The load flow analysis is used to determine the maximum permissible demand by gradually increasing the load until the flow fails to converge. The power system will reach its voltage instability limit when any increase in active or reactive loading demand results in the system operating point crossing the nose of the nose curves. Voltage corresponding to maximum loading point is called as critical voltage.

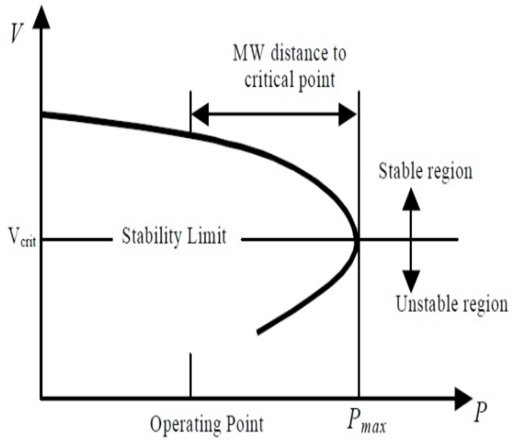

Fig. 2 The P-V curve.

3.1 *Evaluation method*

The transmission expansion planning focuses on improving the load margin of the network. The system loads increasing, and the transmission networks are operating close to their critical point. The effectiveness of the proposed transmission expansion approach on increasing the load margin while satisfying the system reliability criteria are evaluate against the conventional approach. The load margin at each node is determined. Load margin indicates the distance of the load from the base operating point until the critical point. The load margin can be obtained from the nose curve, and it is calculated as shown in equation 9.

$$\text{Load margin} = \mathrm{P_{critical}} - \mathrm{P_{initial}} \tag{9}$$

$\mathrm{P_{initial}}$ is the value of load (MW) at normal operating point and $\mathrm{P_{critical}}$ is the value of load (MW) at voltage collapse point. The network base case is modelled, and the conventional and proposed approaches will be considered for transmission expansion planning. The effectiveness of the approach will be determined. The evaluation method is based on calculating the total system load margin of each approach and their results are compared.

3.2 *Base case consideration*

In implementing the transmission expansion planning, the base case scenario of the operating grid network is considered. It is modelled in PSS®E for load flow analysis. Fig. 3 shows the single line diagram for the grid network system. The power flow results are given in Table A.1.

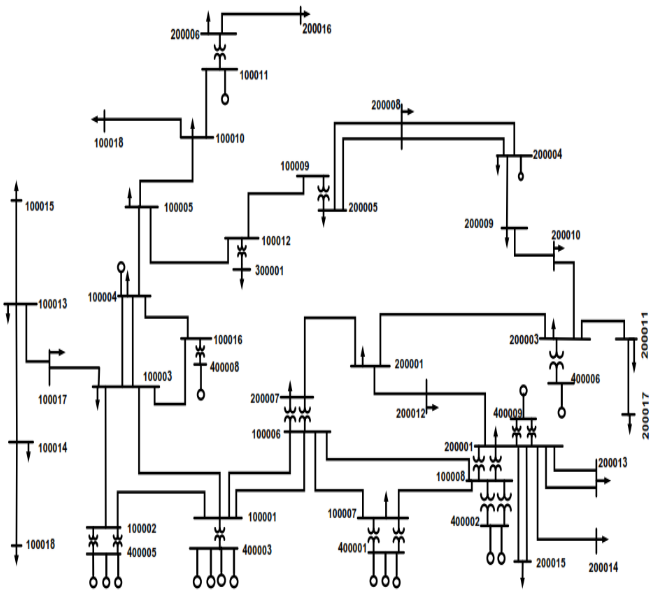

Fig. 3 Base case grid network.

4. Grid network expansion planning by approaches

4.1 *Conventional approach*

This is a normal transmission expansion planning approach used in optimization problems. The objective is to minimize the investment cost while satisfying the system reliability conditions [16,17]. When the power grid is represented by the power flow model, the mathematical model for the transmission expansion planning problem can be formulated as shown in equations 1-5.

The objective function represents the investment cost. The constraint in equations 2,3 and 4 represents the conservation of power in each node. The constraints in equation 5 refers to voltage limits. In obtaining the optimal transmission expansion planning, the grid network is simulated using PSS®E and the simulation results are tested against the objective function as well as the constraints inequalities. The simulation result is given in appendix A in Table A.1.

4.2 *Conventional approach results*

The optimal solution for this network when the AC model is used is given in Table 1. Only seven new transmission lines have been identified for new circuit addition. The circuits for reinforcements are 100007-100020,200002-200003, 200002-200012,200003-200010, 200003-200011, 200004-200009 and 200009-200010.

Table 1 Conventional approach results.

S/N	Transmission line	Cost [$]	Project status
1	100003-100017	29640000	0
2	100006-100007	39216000	0
3	100007-100008	3420000	0
4	100013-100015	34587600	0
5	100013-100017	13748400	0
6	100007-100020	20748000	1
7	200001-200012	8540000	0
8	200002-200003	30625000	1
9	200002-200012	8435000	1
10	200003-200010	12897500	1
11	200003-200011	9275000	1
12	200004-200009	17850000	1
13	200009-200010	19180000	1
14	200011-200017	9275000	0

The results of the proposed transmission lines are indicated in the Fig. 4 below as doted lines.

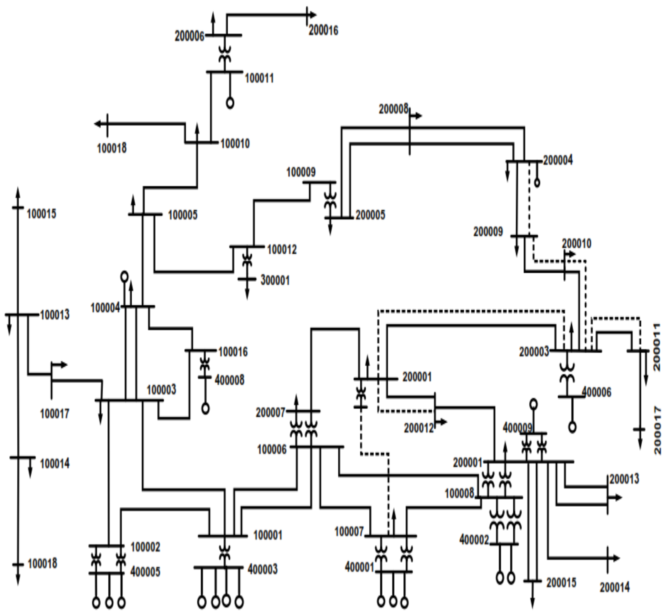

Fig. 4 Conventional approach network results.

The conventional approach in transmission expansion planning does not consider the voltage and active load power complexity towards voltage collapse point.The rate of voltage decline towards critical point is a sensitive constraint in transmission planning. In determining the transmission network configuration, the conventional approach is modified to consider the the relationship of voltage and active power in the system as a planning constraint.

4.3 *Modified conventional approach*

The proposed approach objective is to minimize the investment cost while satisfying the system reliability conditions. The nose curve is considered in this approach to calculate the nose curve index. The index is used as one of the constraints in transmission expansion planning optimization. The mathematical model for the transmission expansion planning problem is reformulated to include the the nose curve index constraint. The optimization is calculated using equations 1-5 and the nose curve index constraint is given by equation 10.

$$\left(\frac{V_i - V_{cr}}{P_L}\right) < 0.01 \qquad (10)$$

The constraint in equations 10 represents the nose curve index at a particular node in the power system where Vcr is the critical bus voltage in pu. The nose curves show the relationship between the power injection and the corresponding change in voltage at a particular bus. The nose curves give the values of voltage stability margin and load margin as shown in Fig. 5 which is a crucial information for the transmission planning. These curves are used to calculate the voltage indices which show the rate of voltage decline with respect to the increment of the real load power. The index considers the nonlinear characteristics of the system and its voltage limits.

The higher the nose curve index the weaker the bus towards voltage collapse and vice versa. When the voltage index becomes large, the system turns insecure and ultimately collapses. The indices for the existing network are shown in Table 2.

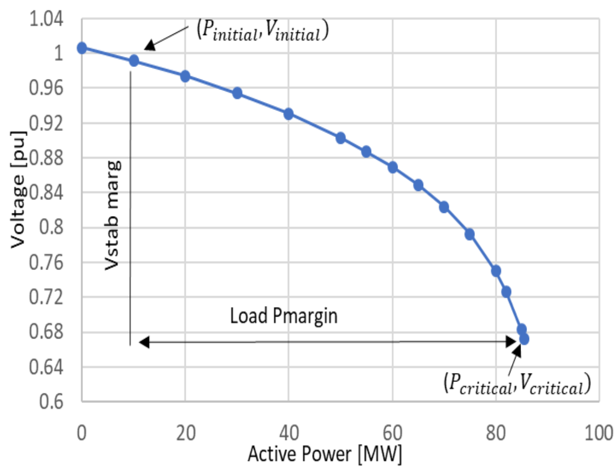

Fig. 5 Nose curve diagram.

Table 2 Nose curve index results.

Bus	Name	$\left(\frac{V_i - V_{cr}}{P_L}\right)$
200017	Tanga	0.0239
200003	Hale	0.0312
200009	Same	0.0424
200012	Mlandizi	0.0123
100017	Mufindi	0.0096
200002	Chalinze	0.0241
200011	Maweni	0.0308
200010	Kasiga	0.0256
100015	Mbeya	0.0024

The transmission expansion planning optimal solution in this approach is obtained by undertaking load flow study of the modeled network using PSS®E and the simulation results are tested against the objective function as well as the given constraints inequalities. The simulation results are given in appendix A in Table A.1.

4.4 *Proposed approach results*

In this approach, the optimal solution for transmission expansion planning is given in Table 3. Only nine new transmission lines have been identified for new circuit addition. The circuits for reinforcements are 100007-100020, 200002-200003,200001-200012,200002-200012,200003-200010, 200002-200012, 200003-200011, 200004-200009 and 200009-200010.

The results of the proposed transmission lines are indicated in the Fig. 6 as doted lines.

Table 3 Proposed approach expansion results.

S/N	Transmission line	Cost [$]	Project status
1	100003-100017	29640000	0
2	200011-200017	9275000	1
3	100006-100007	39216000	0
4	100007-100008	3420000	0
5	200009-200010	19180000	1
6	100013-100015	34587600	0
7	100013-100017	13748400	0
8	100007-100020	20748000	1
9	200001-200012	8540000	1
10	200002-200003	30625000	1
11	200002-200012	8435000	1
12	200003-200010	12897500	1
13	200003-200011	9275000	1
14	200004-200009	17850000	1

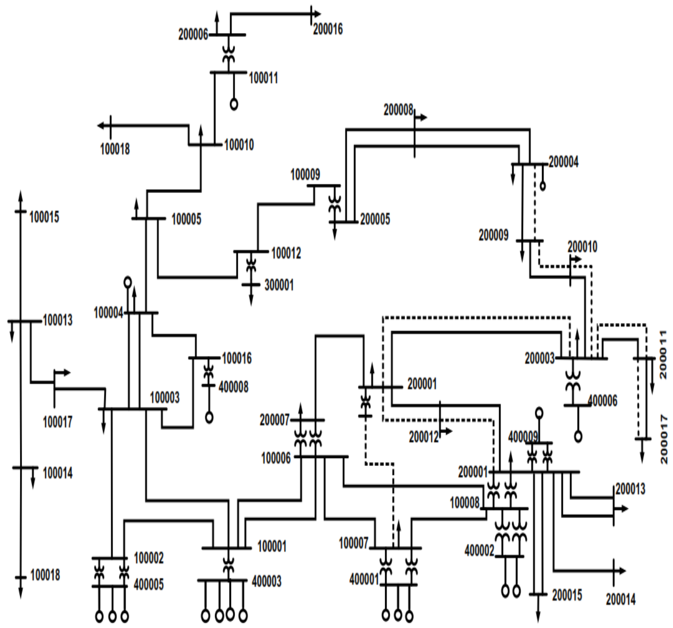

Fig. 6 Expansion planning results by proposed approach.

4.5 *Consideration by comparison*

The conventional approach and proposed approach are evaluated to determine the effectiveness of the approach. The evaluation method is based calculating the total system load margin of each approach and their results are compared. The results are given in Table 4. The results from Table 4 shows that the proposed approach which considers the nose curve index gives 1685MW load margin increase compared to 1596MW load margin provided by the conventional approach. The difference of 85MW is quite significant for voltage stability improvement in constrained transmission network.

Table 4 Calculated load margin at each node.

Bus	Load margin [MW]		
	Base	Conventional	Proposed
200017	73	103	133
200003	116	184	187
200009	80	136	137
200012	230	327	364
100017	121	130	130
200002	234	355	369
200011	94	156	159
200010	82	137	138
100015	66	68	68
$\sum_{i=1}^{N}(Load\ margin)$	1096	1596	1685

The transmission network expansion planning focuses on the improvement of voltage stability of the power system. The proposed approach which considers the nose curve index in its analysis provides an expansion plan with high voltage stability compared to the conventional approach. This is because of the nose curves index which determines the most critical bus to voltage collapse, thus determining the weak nodes in the system as shown in Table 2. The simulation result of the proposed approach is shown in Table A.1 with significant voltage improvement. This information is very crucial for the system planner to make decision on the location of new transmission line connecting the weak bus to other busbars for system reinforcement. Table A.1 in appendix A indicates the resulting voltages obtained when the conventional and proposed approaches are considered in expansion planning. The number of transmission lines to be added, the load margin improvement and their associated costs are shown in Table 5.

Table 5 Approaches comparison.

Approach	Added lines	Load margin [MW]	Cost [$]
Conventional	7	1596	119,010,500
Proposed	9	1685	136,825,500

The proposed approach which considers the nose curve index is an effective tool in transmission expansion planning. The solution which satisfies the index, its transmission network configuration gives high system voltage stability. The solutions which do not satisfy the index inequality; have high nose curve indices, are subjected to voltage instability. They are operating close to the voltage collapse point.

5.Conclusion

The increase of power demand has caused the system to be complex and sensitive to voltage fluctuations. The system experiences voltage instability, line overloading and power system blackouts. The relationship between the load power and the voltage in the power system is very important in transmission expansion planning. There are various approaches deployed to implement the transmission expansion planning optimization.

This paper proposed the simplified approach which considers the nose curve index as a planning tool based on some voltage stability criteria. The voltage stability margin and load power margin increase obtained from the nose curve form a basis for nose curve index calculation. The analysis and consideration performed in this paper has successfully indicated that the proposed approach gives better load margin improvement, and the resulting voltage profile shows significant compliance to the transmission network expansion planning constraints. It is very important to calculate the nose curve index values. This is because accurate nose curve index values are important to determine the capacity and location of transmission line to be added to the existing network.

References

1) Y. A. Mobarak: Voltage collapse prediction for Egyptian interconnected electrical grid EIEG, International Journal on Electrical Engineering and Informatics, Vol. 7, No. 1, pp. 79-88 (2015).
2) P. Kundur *et al*.: Definition and classification of power system stability IEEE/CIGRE joint task force on stability terms and definitions, in IEEE transactions on power systems, Vol. 19, No. 3, pp. 1387-1401 (2004).
3) P. Kundur, J. Paserba and S. Vitet: Overview on definition and classification of power system stability, CIGRE/IEEE PES International Symposium Quality and Security of Electric Power Delivery Systems, pp. 1-4 (2003).
4) M. K. Jalboub, A. M. Ihbal, H. S. Rajamani, R. A. Abd-Alhameed and A. M. Ihbal: Determination of static voltage stability margin of the power system prior to voltage collapse, Eighth International Multi-Conference on Systems, Signals & Devices, pp. 1-6 (2011).
5) P. Kundur: *Power Systems Stability and Control*, 1st edition, McGraw-Hill, New York, p. 27 (1994).
6) S. B. Jitendra and K. D. Chandra: An analysis of different methodology for evaluating voltage sensitivity, IJAREEIE, Vol. 3, Issue 9, pp. 12239-12246 (2014).
7) H. Seif and M. S. Sepasian: *Electrical Power System Planning, Issues, Algorithms, and Solution,* 1st edition, Springer, Berlin, pp. 8-23 (2011).
8) M. Mahdavi and E. Mahdavi: Transmission expansion planning considering network adequacy and investment cost limitation using genetic algorithm, world academy of science, engineering and technology, International Journal of Energy and Power Engineering, Vol. 5, No. 8, pp. 1051-1055 (2011).
9) J. A. Momoh: *Electric Power System Applications of Optimization*, 2nd edition, CRC Press, p. 113 (2019).
10) D. V. Madhava Chary, M. V. Subramanyam and P.

Kishor: P-V Curve method for voltage stability and power margi studies, IJESC, Vol. 7, Issue 5, pp. 11867-11869 (2017).

11) S. Binato, G. C. de Oliveira and J. L. Araujo: A greedy randomized adaptive search procedure for transmission expansion planning, IEEE Trans. Power Systems, Vol. 16, No. 2, pp. 247-253 (2001).

12) G. W. Stagg and A. H. El-Abiad: *Computer Methods in Power System Analysis,* International edition, McGraw-Hill, p. 270 (1985).

13) J. Machowski, Z. Lubosny, J. W. Bialek and J. R. Bumby: *Power System Dynamics Stability and Control*, 3rd edition, Wiley, p. 316 (2020).

14) Y. Wang: Voltage stability assessment using P-Q region incorporating wind power, Theses and Dissertations, p. 176 (2013).

15) G. K. Morison, B. Gao and P. Kundur: Voltage stability analysis using static and dynamic approaches, IEEE Transactions on Power Systems, Vol. 8, No. 3, pp. 1159-1163 (1993).

16) E. Fawwaz and A. Nazih: Power system planning technologies and applications concept, solution, and management, Engineering Science Reference, p. 27 (2012),.

17) S. Lumbreras and A. Ramos: The new challenges to transmission expansion planning survey of recent practice and literature review, Electric Power System Research, Vol. 134, pp. 19-29 (2016).

Appendix A

The load flow simulation is performed using PSS®E for the base case scenario, conventional and proposed approaches. The results are compared against the planning criteria to get the effectiveness transmission network configuration.

Table A.1 Simulation results comparison (Vp.u).

Bus	Base	Conventional	Proposed
100001	1.0346	1.0373	1.0274
100002	1.0347	1.0355	1.0256
100003	1.0485	1.0534	1.0317
100004	1.0546	1.0622	1.0306
100005	1.0226	1.0365	1.0271
100006	1.0145	1.0201	1.0204
100007	0.9916	0.9935	0.9938
100008	0.9862	0.9873	0.9876
100009	0.9831	1.0028	1.0039
100010	1.0165	1.0197	1.0198
100012	0.9832	1.0029	1.0040
100013	1.0203	1.0274	1.0277
100014	1.0399	1.0472	1.0476
100015	0.9713	0.9790	0.9794
100016	1.0503	1.0546	1.0248
100017	1.0246	1.0311	1.0214
100018	1.0417	1.0491	1.0295
100019	1.0046	1.0079	1.0080
100020	0.9990	0.9977	0.9987
200001	0.9501	0.9992	1.0001
200002	0.9680	1.0048	1.0063
200003	0.9987	1.0114	1.0138
200005	0.9559	0.9763	0.9777
200006	1.0012	1.0012	1.0012
200007	1.0018	1.0107	1.0110
200008	0.9559	0.9763	0.9777
200009	0.9661	0.9927	0.9948
200010	0.9661	0.9928	0.9949
200011	0.9803	1.0034	1.0075
200012	0.9474	0.9961	0.9984
200013	0.9450	0.9944	0.9953
200014	0.9439	0.9934	0.9942
200015	0.9386	0.9884	0.9892
200016	0.9800	0.9800	0.9800
200017	0.9676	0.9910	1.0023
300001	0.9761	0.9960	0.9971

Proc. Schl. Eng. Tokai Univ., Ser. E
46 (2021) 15-25
DOI: 10.18995/24343641. 46. 15

A New Approach for Disaster Prediction by Sudden Partial Dam-break Outflow (A Case Study on Amagase Dam)

by

Sayed Masihullah AHMADI[*1] and Yoshimichi YAMAMOTO[*2]

(Received on Apr. 14, 2021, and accepted on June 19, 2021)

Abstract

A two-dimensional (2D) dam-break hydro-morphodynamics simulation model is presented with a newly proposed dam-break outflow rate equation. The results of the proposed new equation are affected by many factors, among which this study evaluated the influence of the dam-break geometry (width and height of a break section) by conducting many dam-breaks experiments in a long, dry-bed, frictionless and rectangular water channel, connected to a finite water reservoir. The hydro-morphodynamics simulation model solves the continuity equation and two-dimensional non-linear shallow water equations for hydrodynamics calculations, and Rebberink's equation and the continuity equation of bed and suspension loads for morphodynamics calculations by using the finite difference method (FDM). Although it is difficult to collect real dam-break data, because both a flood caused by a dam-break and a flood caused by a tsunami are categorized as longwave floods with substantially similar characteristics, to confirm the validity of the hydro-morphodynamics simulation model, the 2011 Great Tohoku Tsunami was simulated on the Sendai-Natori coast of Japan where the results of the simulation came within an acceptable range. Furthermore, to confirm the validity of the proposed dam-break outflow rate equation, Japan's Amagase Dam (an arched concrete dam) was selected for simulating a break; the results of the simulation showed that a flood wave of more than 5 meters in depth could hit the center of Uji City located downstream of Amagase Dam if this dam were to break.

Keywords: Amagase dam, Sudden partial dam-break, hydro-morphodynamics, FDM.

1. Introduction

Dams are constructed to benefit humans by retaining water for different purposes, however, as water is stored behind a dam, enormous potential energy is formed that in the case of a dam-break, devastating catastrophe may follow, especially, when densely populated cities are located downstream of a dam. Dam-break can happen due to many different reasons, varying from natural causes like mega earthquakes, heavy flash floods, etc., to the aging of the dam, miscalculations, or even human attributes like terrorist attacks, wars, and sometimes, major construction projects can increase the potential threats of a dam-break. (You et al., 2012)[1). Therefore, in this paper, the authors present a simplified dam-break outflow rate concept applicable for break simulations of nonerodable dams assuming a sudden-partial break. The proposed concept is then installed on an existing model that is based on the finite-difference method that can be used by the researchers and consultants of the field. Therefore, it is the main objective of the current publishing. In the literature, dam-break simulation consists of routing the inflow flood through a reservoir, estimating the dam breach characteristics, and downstream flood routing/modeling ("Using HEC-RAS for Dam Break Studies," 2014)[2) out of which, the two primary tasks in the hydraulic analysis of a dam-break are the prediction of the reservoir outflow hydrograph and the routing of this boundary condition through the tailwater areas (Pilotti et al., 2010)[3). The dam-break outflow hydrograph depends on the construction material of a dam and the type of breach, however, generally speaking, a hydrograph is affected by the bathymetry of a dam, valley shape, dam height, and shape and extension of the breach, therefore, one can find many research reports of the type (Pilotti et al., 2010)[3), (Saberi and Zenz, 2015)[4), (Basheer et al., 2017)[5), (Hakimzadeh et al., 2014)[6). Even though there is a broad amount of research on the topic of dam-break, but because of the complexity of the phenomenon, it is very difficult to anticipate a dam breach formation. However, in this paper, the authors intend to simulate arch-action concrete dams that fail instantaneously

*1 Graduate student, Architecture and Civil Engineering Course, Graduate School of Science and Technology,
*2 Professor, Department of Civil Engineering

and this type of breach formation simulation is not covered here. Furthermore, the authors have developed a new dam-break outflow-rate equation. The proposed equation has many variables out of which, the influence of the dam-break height and width on the out-flow hydrograph is investigated through many hydraulic experiments, and a suitable coefficient for this attribute is developed, consequently, this outflow equation is integrated into a two-dimensional flood simulation model of Ca et al. (2010)[7]. This model uses the two-dimensional (2D) non-linear shallow water equations and continuity equation for hydrodynamics calculations and the Rebberink's formula (Rebbenrink et al., 1998)[8] for modeling sediment transport. Because the data of a real dam-break is very difficult to achieve (He et al., 2020)[9], the validity of this model for a long wave flood routing was previously investigated by performing tsunami simulations on the Sendai-Natori coast of Japan, where, it experienced the 2011 Great East Japan Tsunami. (Ahmadi et al., 2020)[10]. Moreover, as a case study, the dam-break simulation to Amagase Dam located upstream of a population center of Uji City in Japan is executed and the results depicted that a flood wave of more than 5 meters in-depth, with a velocity of about 6 meters per second will possibly hit the downstream and if proper mitigations are not considered, devastating might follow.

2. Calculations

2.1 *Existing Numerical Simulation Model*

For the prediction of the topographical change by the tsunami, the numerical simulation model of Ca et al. (2010)[7] is used. The model was developed using the following detailed formulas.

2.1.1 *Numerical Model for Fluid Motion*

The numerical model used for tsunami simulations in this paper is based on a continuity equation of fluid (Eq. 1) and two-dimensional nonlinear long-wave equations (Eqs. 2 & 3), and these governing equations are solved by finite difference method using the Crank-Nicholson scheme.

$$\frac{\partial f_y q_x}{\partial x}+\frac{\partial f_x q_y}{\partial y}+\frac{\partial S\eta}{\partial t}=0 \tag{1}$$

$$\begin{aligned}&\frac{\partial q_x}{\partial t}+\frac{1}{S}\frac{\partial}{\partial x}\left(\frac{Sq_x^2}{d}\right)+\frac{1}{S}\frac{\partial}{\partial y}\left(\frac{Sq_xq_y}{d}\right)+\\ &\quad gd\frac{\partial \eta}{\partial x}-\frac{1}{S}\frac{\partial}{\partial x}\left[d\nu_t S\frac{\partial(q_x/d)}{\partial x}\right]-\\ &\quad\frac{1}{S}\frac{\partial}{\partial y}\left[d\nu_t S\frac{\partial(q_x/d)}{\partial y}\right]+\frac{f_c}{d^2}Qq_x=0\end{aligned} \tag{2}$$

$$\begin{aligned}&\frac{\partial q_y}{\partial t}+\frac{1}{S}\frac{\partial}{\partial x}\left(\frac{Sq_yq_x}{d}\right)+\frac{1}{S}\frac{\partial}{\partial y}\left(\frac{Sq_y^2}{d}\right)+\\ &\quad gd\frac{\partial \eta}{\partial y}-\frac{1}{S}\frac{\partial}{\partial x}\left[d\nu_t S\frac{\partial(q_y/d)}{\partial x}\right]-\\ &\quad\frac{1}{S}\frac{\partial}{\partial y}\left[d\nu_t S\frac{\partial(q_y/d)}{\partial y}\right]+\frac{f_c}{d^2}Qq_y=0\end{aligned} \tag{3}$$

Here, q_x & q_y are the horizontal fluid fluxes in the x & y directions respectively. η is the water surface elevation. f_x & f_y are the x & y direction ratios of the wet portion in a calculation mesh. S is the area ratio of the wet portion in a calculation mesh. d is the water depth (from the static water surface+ η). g is the gravitational acceleration. ν_r is the eddy viscosity coefficient. f_c is the ground surface friction coefficient, and $Q\left(=\sqrt{q_x{}^2+q_y{}^2}\right)$ is the compound value of q_x & q_y. To calculate the eddy viscosity coefficient and the ground surface friction coefficient, the following equations are used;

$$\nu_r=\varepsilon\left[\left(\frac{\partial U}{\partial y}\right)^2+\left(\frac{\partial V}{\partial x}\right)^2\right]^{1/2}\cdot d^2 \tag{4}$$

$$f_c=\frac{gn^2}{d^{1/3}}\quad,\qquad n^2=n_0{}^2+0.020\frac{B_r}{100-B_r}d^{4/3}\quad,$$

$$n_0{}^2=\frac{(n_1)^2A_1+n_2{}^2A_2+n_3{}^2A_3}{A_1+A_2+A_3} \tag{5}$$

Here, U and V are the flow velocity in y and x directions. ε equals (0.1). n is Manning's roughness coefficient. B_r is the building ratio (= the ratio of the area of all vertical objects like houses and trees to the mesh area). n_0 is the weighted average roughness coefficient of areas like farms, roads, and waste & wetlands, $A_{1,2,\&3}$, with relative roughness coefficients of $n_{1,2,\&3}$.

2.1.2 *Numerical Model for Topographical Change*

The topographical change based on sediment transport by the flow can be expressed by using the continuity equation, (Eq. 6).

$$\frac{\partial \zeta}{\partial t}=-\frac{1}{1-\varepsilon_s}\left(\frac{\partial q_{bx}}{\partial x}+\frac{\partial q_{by}}{\partial y}-C_s+C_{ut}\right) \tag{6}$$

Here, ζ is the ground surface elevation, q_{bx} & q_{by} are respectively the bed-load rate per unit width in x & y directions, C_s is the deposition rate of the suspended load, C_{ut} is the entrainment rate of the suspended load from the bed, and ε_s is the porosity of the sediment. For a detailed illustration of the equations in this section, please refer to Ahmadi et al. (2020)[10].

- ***Modeling of q_x & q_y on Bed-load Transport***

For evaluation of the bed-load rate, Ribberink's formula (1998)[8] shown in (Eq. 7) is used. Yokoyama et al. (2002)[11] performed many calculations of scouring by flow & wave using indoor and outdoor data on sand & gravel with the diameter range of 0.2~10 mm and found that accurate results can be obtained using this formula.

$$q_{bi} = \begin{cases} C_b[|\theta_s(t)| - \theta_{sc}]^{1.65} \frac{\theta_s(t)}{|\theta_s(t)|} \sqrt{\Delta g D_{50}} & (\theta_s(t) \geq \theta_{sc}) \\ 0 & (\theta_s(t) < \theta_{sc}) \end{cases} \quad (7)$$

Here, q_{bi} is the bed-load transport rate per unit width in the i direction, C_b is the bed-load coefficient determined by verification simulations, however, the authors by performing many hydraulic experiments, developed useful diagrams to acquire the value of this coefficient, Figs. (3-5) (Ahmadi et al., 2020)[10], $\theta_s(t)$ is the Shields parameter in the i direction, θ_{sc} is the critical Shields number, Δ is the relative density of the sand, g is the gravitational acceleration, D_{50} is the median diameter of the sediment.

2.2 *New Model of Dam-break Out-flow Rate*

The cause for a dam-break is varied in each dam-break case where the most common causes can be great earthquakes, overtopping due to heavy flash floods (this failure impetus is expected to increase in the following decades due to climate changes), and the aging of a dam. A more complete list of the most prominent causes of dam-break are listed in the US Army Corps of Engineers Hydrologic Engineering Center, Flood Emergency Plans, Guidelines for Corps Dams as (1) Earthquake; (2) Landslide; (3) Extreme storm; (4) Piping; (5) Equipment malfunction; (6) Structure damage; (7) Foundation failure; (8) Sabotage (Owen et al., 1980)[12]. For every dam failure, there might be a different breach formation shape and time that makes a dam-break simulation and accurate calculations very complex. In the literature, many researchers have so far developed models to simulate the dam breach scenarios on different types of dams and as well as different failure cases. "Methodology for Earthen Dam Breach Analysis" (Yue Sheng et al., 2016)[13], "Hydrodynamic Dam Breach Modelling of Earthfill Saddle Dam" (Sidek, 2011)[14], "Analysis of Hydrograph by Dam Breach Shapes" (ki-bum Park, 2019)[15] are some of the researches which concentrate more on the failure shapes and the discharge rates of different dam type's failure with various break sections, however, in this paper, the main focus is flood routing and morpho-dynamics calculations following a dam-break. For this purpose, we have assumed a trapezoidal break section for a dam-break shown in Figs. 1&2 and derived new equations for calculating a run-off rate to this dam-break shape as illustrated in the following;

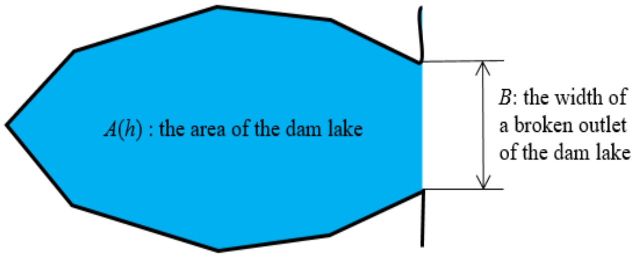

Fig. 1 Plan view of the dam lake.

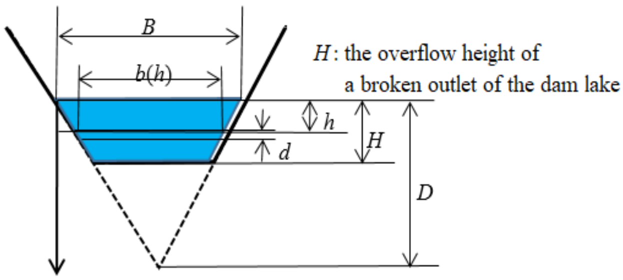

Fig. 2 Dam-break section view.

The run-off rate from the dam lake in the case that the overflow height H is constant (water supply is infinite) can be calculated from bellow equations;

$$Q_r = \int_0^H b(h) \times c\sqrt{2gh}\, dh = \int_0^H \frac{B(D-h)}{D} c\sqrt{2gh} dh \quad (8)$$

$$Q_r = \frac{B}{D} c\sqrt{2gh} \left[D\frac{2}{3} h^{3/2} - \frac{2}{5} h^{5/2} \right]_0^H \quad (9)$$

$$Q_r = \frac{B}{D} c\sqrt{2g} \left(\frac{2}{3} D H^{3/2} - \frac{2}{5} H^{5/2} \right) \quad (10)$$

Here, Q_r is the discharge rate.

Since the case of finite water supply from a dam lake is more realistic in the actual dam-break cases, in this paper, we have used the equation for run-off rate from the dam lake by the following equations;

$$Q_r = A(h) \times \frac{dh}{dt} \quad (11)$$

$$Q_r = \frac{B}{D}c\sqrt{2g}\left(\frac{2}{3}D\left(H-\frac{dh}{dt}T\right)^{3/2} - \frac{2}{5}\left(H-\frac{dh}{dt}T\right)^{5/2}\right) \tag{12}$$

Here, T is the run-off elapse time (sec), V is the total volume of discharge water, and c is the flow rate coefficient.

$$V = \int_0^H A(h)dh = \int_0^{\frac{H}{dh/dt}} Q dT \tag{13}$$

$$V = \int_0^{\frac{H}{dh/dt}} \frac{B}{D}c\sqrt{2g}\left(\frac{2}{3}D\left(H-\frac{dh}{dt}T\right)^{3/2} - \frac{2}{5}\left(H-\frac{dh}{dt}T\right)^{5/2}\right)dT \tag{14}$$

$$= \frac{B}{D}c\sqrt{2g}\frac{-1}{dh/dt}\int_H^0\left(\frac{2}{3}DX^{3/2} - \frac{2}{5}X^{5/2}\right)dX \tag{15}$$

$$= \frac{B}{D}c\sqrt{2g}\frac{-1}{dh/dt}\left[\frac{4}{15}DX^{5/2} - \frac{4}{35}X^{7/2}\right]_H^0 \tag{16}$$

$$Here, X = H - \frac{dh}{dt}T \ , \frac{dX}{dT} = -\frac{dh}{dt} \tag{17}$$

$$T = 0 \rightarrow T = \frac{H}{dh/dt}, X = H \rightarrow X = 0 \tag{18}$$

Thus,

$$\therefore V = \frac{B}{D}c\sqrt{2g}\frac{+1}{dh/dt}\left(\frac{4}{15}DH^{5/2} - \frac{4}{35}H^{7/2}\right) \tag{19}$$

$$\therefore \frac{dh}{dt} = \frac{Bc\sqrt{2g}}{DV}\left(\frac{4}{15}DH^{5/2} - \frac{4}{35}H^{7/2}\right) \tag{20}$$

$$\therefore T_{total} = \frac{H}{dh/dt} = \frac{DV}{Bc\sqrt{2g}}\frac{1}{\frac{4}{15}DH^{5/2} - \frac{4}{35}H^{7/2}} \tag{21}$$

Here, D is the imaginary depth from the dam crown height and it is assumed many times the depth of a dam in this simulation.

3. Evaluation Methods of Empirical Coefficients

3.1. *Rational Evaluation of the Coefficient of Bed-load Transport Rate*

To calculate the bed-load transportation, the model of Ca et al. uses Rebberink's formula (Eq. 7). To use this equation, one needs to calculate its c_b value using the graphs provided in Figs. 3-5 as well as (Eq. 22). The presented graphs and illustrations of their production and use are detailed in the research of Ahmadi et al. (2020)[10].

$$C_b = C_{bo} \times C_1 \times C_2 \tag{22}$$

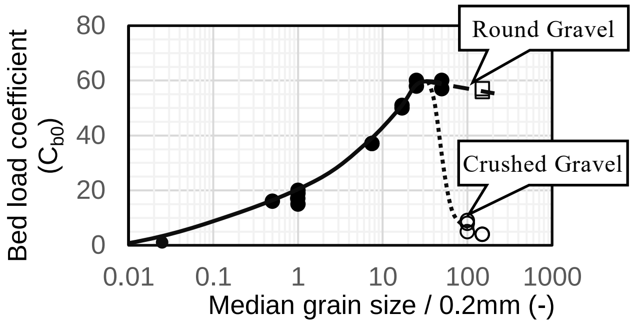

Fig. 3 Influence of the median grain size to the bed-load coefficient.

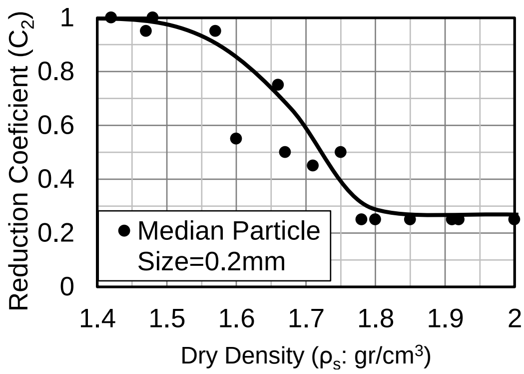

Fig. 4 Influence of dry density to the bed-load reduction coefficient (the median grain size & the uniformity coefficient are 0.2 mm & 20.1).

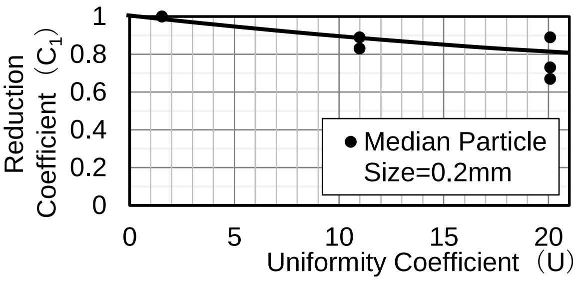

Fig. 5 Influence of the uniformity coefficient to the bed-load reduction coefficient (the median grain size is 0.2 mm, dry densities are around 1.5 g/cm^3).

3.2 *Evaluation of the coefficient of the outflow rate*

For the newly proposed outflow rate equation, (Eq. 12), the coefficient c has a great impact on a calculated hydrograph. This coefficient depends on many variables i.e., dam bathymetry, type of break, break dimensions, and dam width and height. Initially, the dam-break section's impact on this coefficient is evaluated in this paper, by performing many hydraulic experiments. Figs. 6 & 7 shows the apparatus and experimental arrangements respectively, on the left-hand side of the apparatus, there is a water tank reserve as a dam reservoir, at the downstream, there is a dry-bed water channel of 0.5m in width, 0.5m in height, and 9.5 m in length. At the one-meter section from the reservoir, two layers of acryl plates of one centimeter in thickness are placed. The two plates are arranged as one of them is cut to the desired section and the other one acts as a gate. The first acryl plate is glued to the water channel by silicon and the other acryl plate (the gate) is placed before the first plat and there, grease is used as a lubricant in between the plates to let us open the gate abruptly. This complies with our objective of sudden partial dam-break. From these experiments, we intend to develop the hydrographs, therefore, using a digital camera that is focused on the scale bar located about 50 centimeters upstream of the acryl plates, the whole process of the experiments is recorded.

Using this arrangement, one can measure the change in water height behind the dam, and because previously, the bathymetry measurements (reservoir surface area) are taken, the discharge rate is calculated. Fig. 8, shows the calculated and measured hydrographs. For calculated hydrographs, the c value is set as to make the best fit curve in respective to the measured data best-fit curve, as a result, the best value of c is acquired. The experimental data and their results are shown in Table 1.

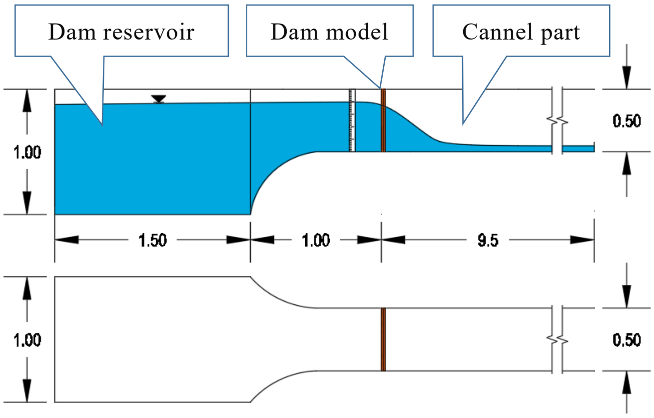

Fig. 6 Dam-break experiment apparatus.

Fig. 7 Dam-break experiment in a rectangular channel.

Because in each of the experimental cases, a different value of c is acquired, an average value of this coefficient is calculated to be 0.28 and It is used for dam-break simulations of the Amagase dam illustrated in the subsequent sections of this paper.

Table 1 Dam-break experiment data and results.

Case	Description	Break dimensions			c
		B (m)	H (m)	Break section thickness (cm)	
I.1	Trapezoidal	0.3	0.25	1	0.30
1.2	Trapezoidal	0.3	0.25	1	0.30
2.1	Trapezoidal	0.3	0.25	1	0.20
2.2	Trapezoidal	0.3	0.25	1	0.20
3.1	Trapezoidal	0.2	0.3	1	0.35
3.2	Trapezoidal	0.2	0.3	1	0.35
4	Triangle	0.2	0.3	0.2	0.50

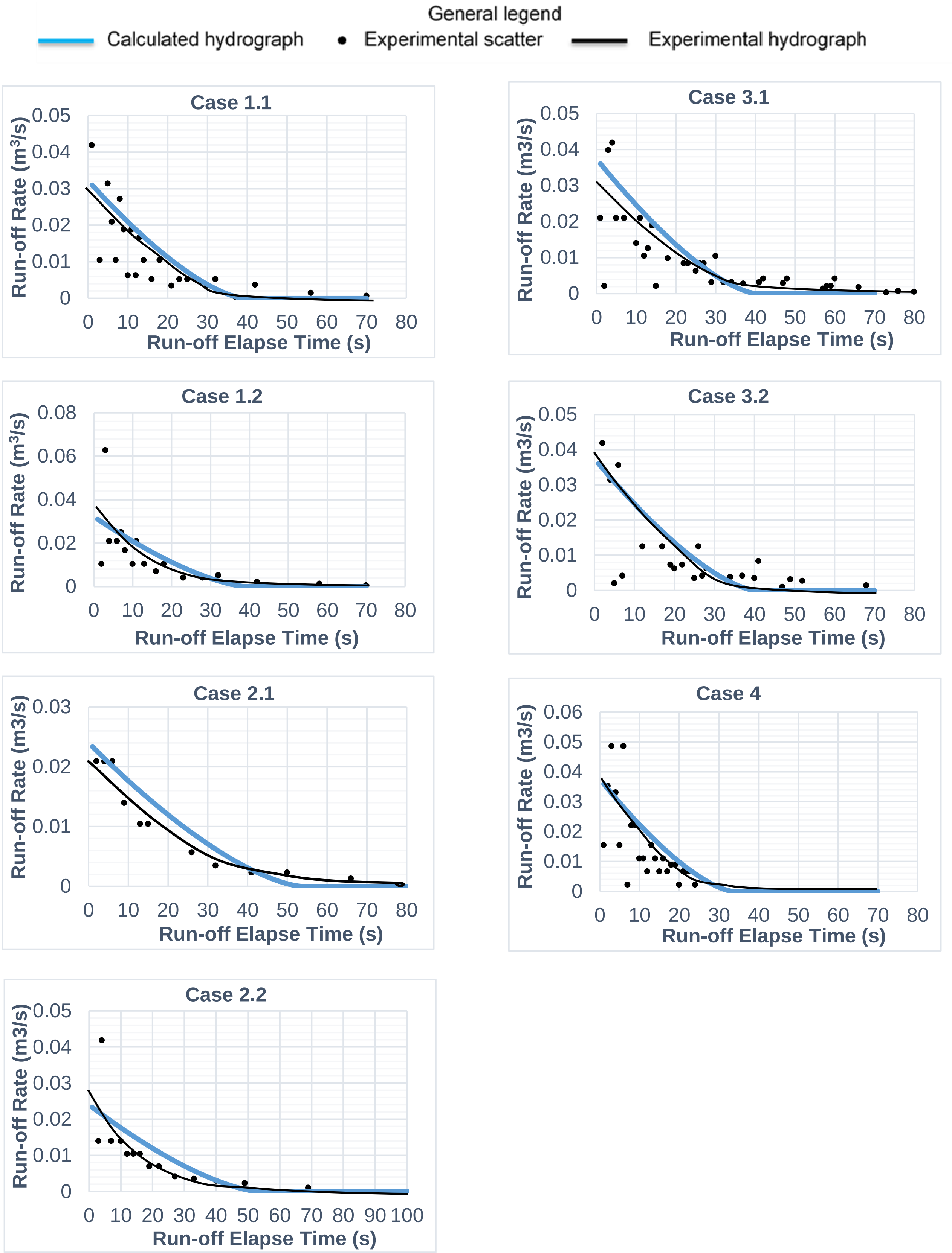

Fig. 8 Dam-break hydrographs from experimental cases and calculated using Eq. 12 (Case 1-4).

4. Verification Simulations

4.1 *Hydro-morphodynamics Simulation in Sendai-Natori Coast*

Sendai-Natori coast is located in the Miyagi prefecture of Japan. This coast experienced a magnitude 9.0 earthquake and a consequent catastrophic great tsunami in 2011. The authors executed many hydro-morphodynamics simulations to replicate the actual flooding conditions and presented the results on the paper (Ahmadi et al., 2020)[10]. The authors also showed in their paper that the results of the simulations are in good agreement with the actual measured data from the area as shown in Fig. 9(a), random spot elevation-change points are selected and their relative data are plotted from both measured data and the reproduction data along line (A) shown on Fig. 9(b). For the locations where measured data is available, the calculated data matches perfectly with the measured data, however, for some locations like the seaside or underwater parts, because there is no digital elevation model data available, one cannot decide whether it differs from the actual topography change situation.

4.2. *Dam-break Hydro-morphodynamics Simulation of Amagase Dam*

Amagase Dam is located in Uji City in Kyoto Prefecture of Japan shown in Fig. 10. It is an arch dam made of concrete, built on the Uji-Gawa river shown in Fig. 11. The Amagase dam's construction started in 1955 and finished in 1964. This dam is mainly constructed for flood control and It also serves as a great water supply reservoir for the Uji City residents. The catchment area of the dam is 4200 square kilometers and its design volume is 122 thousand cubic meters. The height of the dam is 73 meters with a crest length of 254 meters. The reason behind why this dam is chosen for simulation is, about 200 thousand people live downstream of the dam and if in a worst-case scenario this dam, breaks, it would be catastrophic. Therefore, in this paper, it is intended to prepare a hazard map to depict the inundation height, velocity, scouring, and deposition depths for the possible affected area. For the proposed dam-break simulation, the following information is required as input data sets; (1) Assumed broken width and height, (as listed in Table 2). (2) Proposed dam's reservoir area, (as listed in Table 2). (3) Water head behind the dam, (as listed in Table 2). (4) Calculation meshes size, (as listed in Table 2). Because the proposed model of Ca et al. (2010)[7] is based on the finite difference method (FDM), the mesh size limitation is always a concern which mainly depends on the capacity of the available computer, size of the proposed dam, and required accuracy. (5) Existing topography contour map as shown in Fig. 12, in this research, a 10-meter accuracy digital elevation map (DEM) is used. (6) The building and trees ratio in a mesh

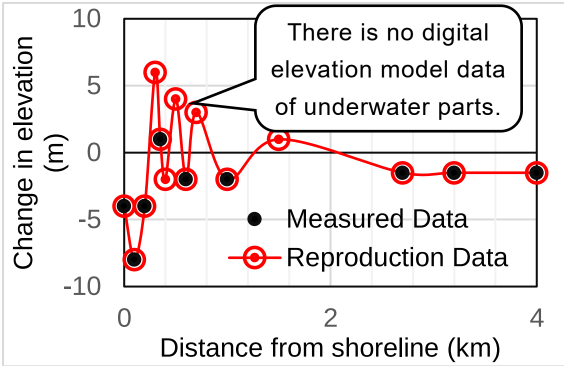

Fig. 9(a) Relative accuracy of the topography-change along line (A) on the measured and reproduced simulation results.

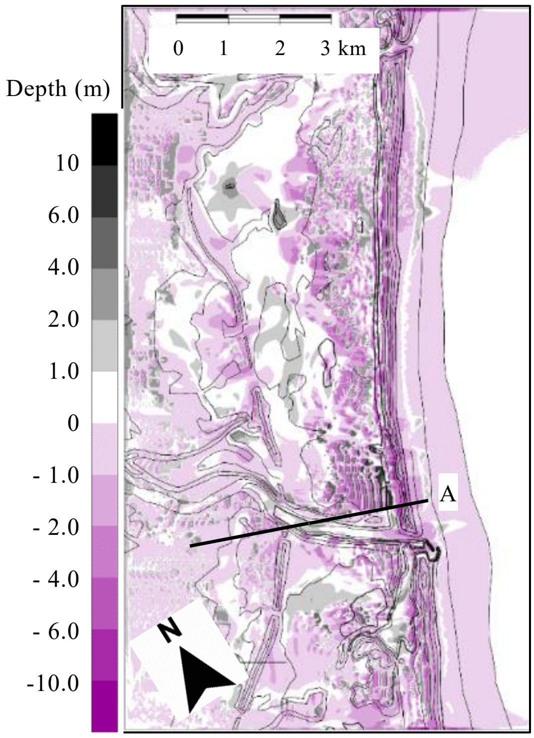

Fig. 9(b) Topography change results (Total bed - load), 48 minutes from start of the tsunami calculations.

as shown in Fig. 13, the light green color (the building ratio is 1 % in a mesh area) is referend to a soil and sand area, the dark green color (5 % in a mesh area) shows a wood area and a forest area, the light brown (30 % in a mesh area) shows a house with a garden, the gray color area (70 % in a mesh area) shows a building area, (7) Grain size distribution in the area, and (8) Calculation limit boundary.

Table 2 Input data for dam-break simulation.

Description	Value
Broken width and height (m)	100 X 50
Broken area (sq. m)	2500
Dam reservoir area (sq. m)	1’880’000
Water height behind the dam (m)	68
Mesh size (m)	20 X 20

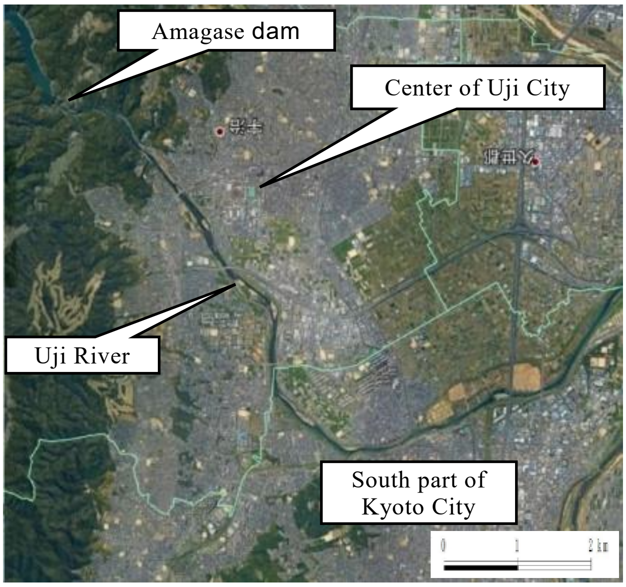

Fig. 10 Locations of Amagase Dam and the high-density zone of the population of Uji City (the gray zone is the circumference of “Center of Uji City”).

Fig. 11 A photo of Amagase Dam (the dam height is 73m, the dam width is 254m).

The results of the Amagase dam-break simulation are shown in Figs. 14-22. Scouring depths and deposition heights are depicted in Figs. 14-16. The maximum scouring depth is about 10 meters close to the dam and it decreases to about 5 meters as the bore reaches further locations from the dam. Forward and return velocity distributions are depicted in Figs. 17-19, the maximum forward velocity is calculated to be about 6 meters per second and the maximum return velocity is found

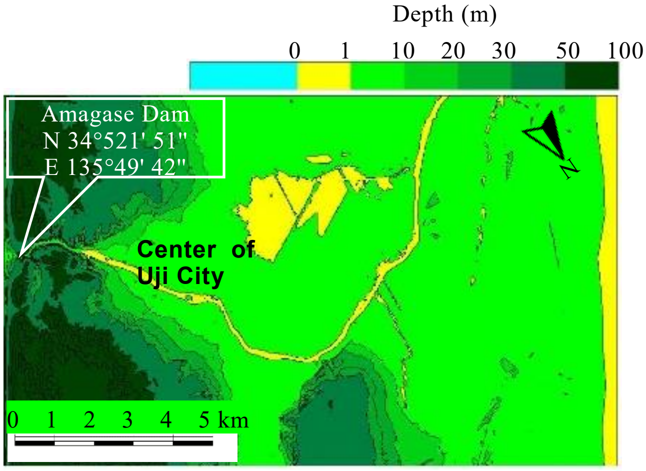

Fig. 12 Existing topography – Downstream of Amagse dam (Uji City).

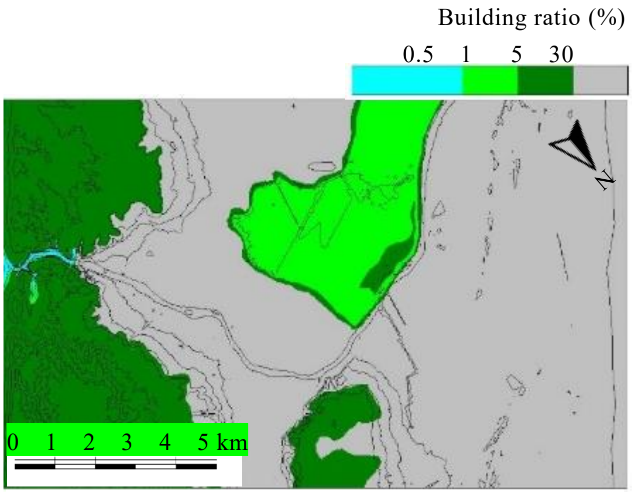

Fig. 13 Building ratio in a calculation mesh (= the area ratio of buildings & trees in a mesh).

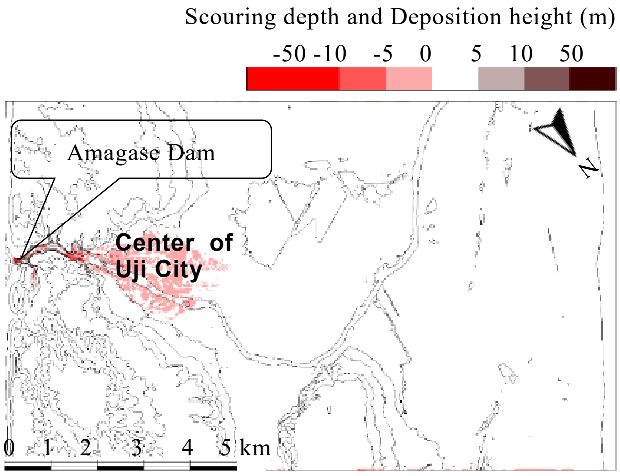

Fig. 14 Topography change, 10 minutes after the start of the calculation.

to be 3 meters per second. Inundation height and extent are depicted in Figs. 20-22.

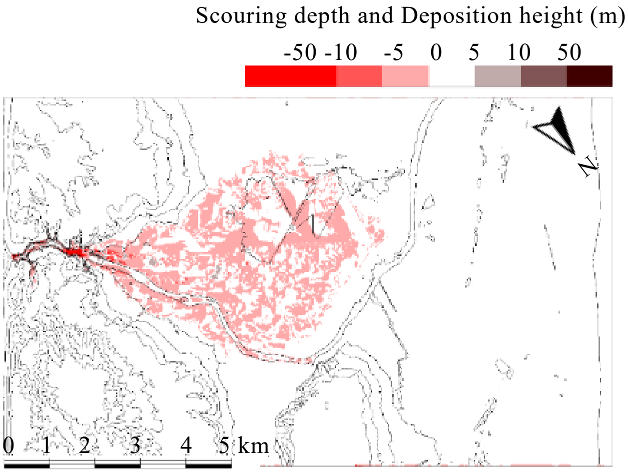

Fig. 15 Topography change, 20 minutes after the start of the calculation.

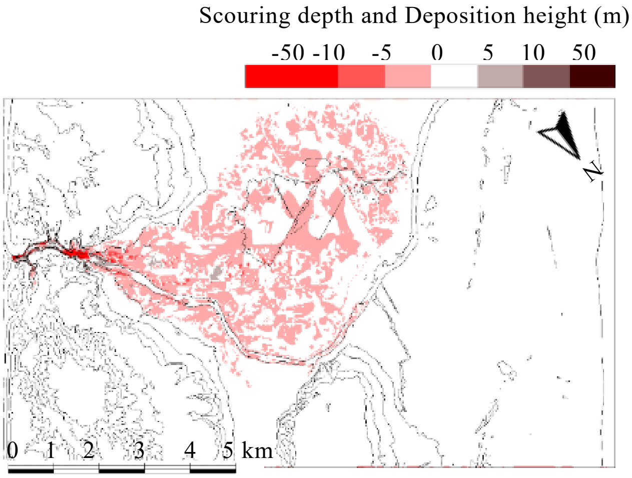

Fig. 16 Topography change, 30 minutes after the start of the calculation.

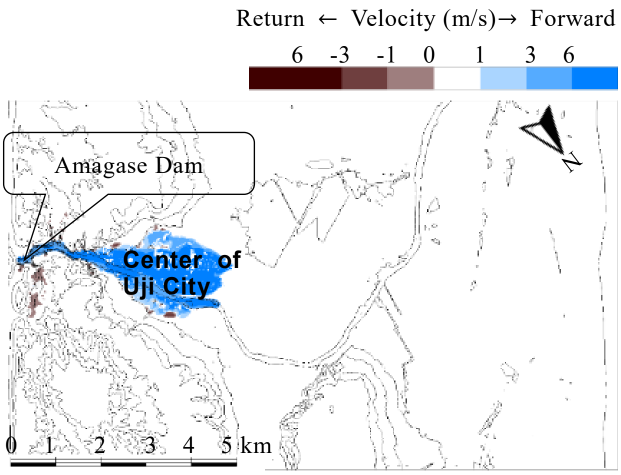

Fig. 17 Inundation velocity, 10 minutes after the start of the calculation.

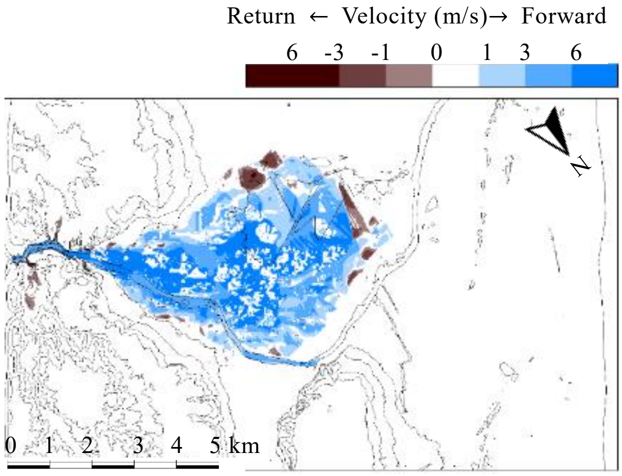

Fig. 18 Inundation velocity 20 minutes after the start of the calculation.

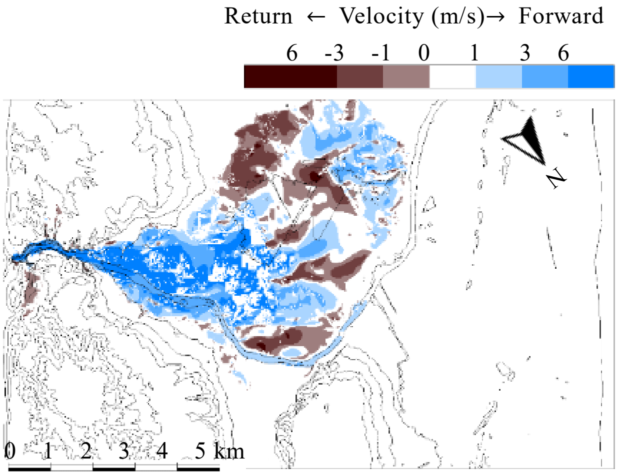

Fig. 19 Inundation velocity 30 minutes after the start of the calculation.

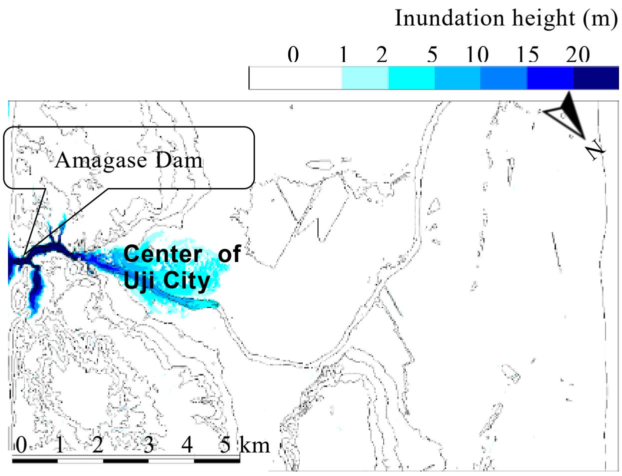

Fig. 20 Inundation height, 10 minutes after start of the calculation.

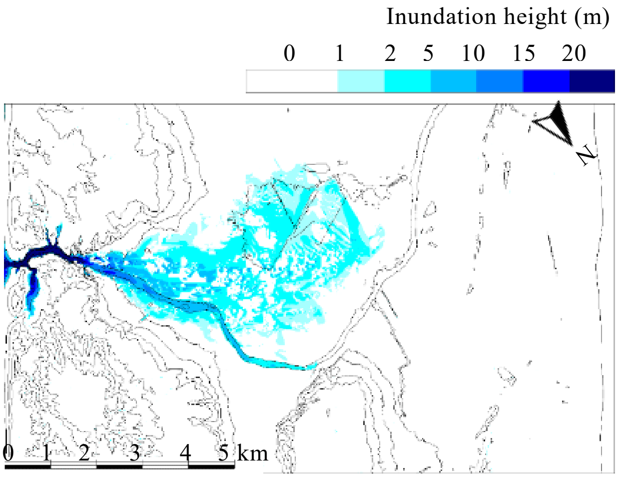

Fig. 21 Inundation height, 20 minutes after start of the calculation.

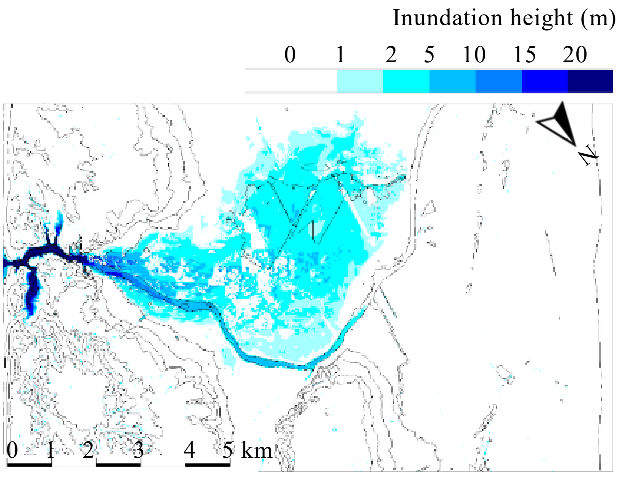

Fig. 22 Inundation height, 30 minutes after start of the calculation.

5. Conclusion

A new approach towards a dam-break hydro-morphodynamics simulation is present with a simple and user friendly manner. Furthermore, a new dam-break outflow rate equation is also presented. The proposed outflow rate equation's output depends on many variants, i.e., bathymetry, dam height, breach shape, and characteristics, etc., out of which, the inference of a dam breach shape (break section's height and width) are evaluated by performing many hydraulic experiments in a rectangular water channel. By comparing the experimental and calculated hydrographs, and trial-error practice, a best fitting curve is acquired with a proper coefficient c, consequently, by integrating the proposed outflow rate equation on a two-dimensional flood simulation model, and simulating the Amagase dam-break, it is perceived that this equation can be potentially useful for the preparation of dam-break flood routing. According to the simulation results of the Amagase Dam presented in this paper, thousands of lives, as well as a countless amount of economy, is in a high-risk zone in case of a dam-break, therefore, the authors suggest that the households living downstream of the Amagase dam and in the high-risk zone, should be informed of the potential danger. In the case of superannuated dams in the area where the frequency of Mega Earthquakes is high, a brief hazard map would be useful for all dams in the area especially the Amagase dam that a densely populated city is right at its downstream. By widening the Amagase dam and by the improvement of dikes at certain locations, the risk of calamity can be lowered.

References

1) L. You, C. Li, X. Min, and T. Xiaolei: Review of Dam-break Research of Earth-rock Dam Combining with Dam Safety Management. Procedia Eng. 28 (2012), 382–388, https://doi.org/10.1016/j.proeng.2012.01.737.

2) US Army Corps of Engineers (USACE): *Using HEC-RAS for Dam Break Studies*, (Institute for Water Resources Hydraulic Engineering Center, 609 Second Street, Davis, Ca 95616-4687, 2014).

3) M. Pilotti, M. Tomirotti, G. Valerio, and B. Bacchi: Simplified Method for the Characterization of the Hydrograph following a Sudden Partial Dam Break, J. Hydraul. Eng. 136 (2010), 693–704, https://doi.org/10.1061/(ASCE)HY.1943-7900.0000231.

4) O. Saberi and G. Zenz: Empirical Relationship for Calculate Outflow Hydrograph of Embankment Dam Failure due to Overtopping Flow, Int. J. Hydraul. Eng. 9 (2015), https://doi:10.5923/j.ijhe.20150403.01.

5) T. A. Basheer, A. Wayayok, B. Yusuf, and R. Kamal: Dam breach parameters and their influence on flood hydrographs for Mosul dam, J. Eng. Sci. Technol. 12 (2017), 14.

6) H. Hakimzadeh, V. Nourani, and A. B. Amini: Genetic Programming Simulation of Dam Breach Hydrograph and Peak Outflow Discharge, J. Hydrol. Eng. 19 (2014), 757–768, https://doi.org/10.1061/(ASCE)HE.1943-5584.0000849.

7) V. T. Ca, Y. Yamamoto, and N. Charusrojthanadech: Improvement of Prediction Methods of Coastal Scour and Erosion due to Tsunami Back-flow, Proc. 20th Intl. Offshore and Polar Engineering Conference (2010), 1053-1060.

8) J. S. Ribberink: Bed-load Transport for Steady Flows and Unsteady Oscillatory Flows, Coastal Engineering 34 (1998), 59-82.

9) G. He, J. Chai, Y. Qin, Z. Xu, and S. Li: Evaluation of Dam Break Social Impact Assessments Based on an

Improved Variable Fuzzy Set Model, Water 12 (2020), https://doi.org/10.3390/w12040970.

10) S. M. Ahmadi, Y. Yamamoto, and V. T. Ca: Rational Evaluation Methods of Topographical Change and Building Destruction in the Inundation Area by a Huge Tsunami, J. Mar. Sci. Eng. 8 (2020), https://doi.org/10. 3390/jmse8100762.

11) Y. Yokoyama, H. Tanabe, K. Torii, F. Kato, Y. Yamamoto, J. Arimura, and V. T. Ca: A quantitative valuation of scour depth near coastal structures, Proc. ICCE2002 (2002), 1830-1841.

12) H. J. Owen: *Flood Emergency Plans*: *Guidelines for Corps Dams*, (Fort Belvoir, VA, Defense Technical Information Center, 1980), http://www.dtic.mil/docs/citations/ADA158679.

13) S. Yue, E. Damisse, and M. Ansar: Methodology for Earthen Dam Breach Analysis, World Environmental and Water Resources Congress, May 22–26, West Palm Beach, Florida (2016).

14) L. Y. Sidek1, F. C. Ros, N.N.N. Ibrahim, A.Z.A. Razad, M.N. Ahmad: Hydrodynamic Dam Breach Modelling of Earthfill Saddle Dam, Journal of Energy & Environment 3 (2011) No. 1, 28-32.

15) Ki-Bum Park: Analysis of Hydrograph by Dam Breach Shapes, Journal of the Environmental Sciences 16 (2007) No 4, 487-493.

Proc. Schl. Eng. Tokai Univ., Ser. E
46 (2021) 27-36
DOI: 10.18995/24343641.46.27

Energy Harvesting Characteristics of Electricity Generation System with Piezoelectric Element under Random Excitation

by

Hiroyuki MORIYAMA[*1], Hirotarou TSUCHIYA[*2] and Helmut Takahiro UCHIDA[*3]

(Received on Mar. 31, 2021 and accepted on Jul. 8, 2021)

Abstract

In this study, a circular plate that is installing a piezoelectric element at its center is adopted as energy-harvesting system and is subjected to a harmonic point force. To assume the application of this electricity generation system to actual environment, the point force, whose frequency is different from the natural frequency, is added to the harmonic point force. Then the excitation force ratio, which is determined by dividing the additional point force by the original point force, is defined. The mechanical power supplied to the plate, the electric power in the electricity generation and the electricity generation efficiency derived from those powers are considered as electricity generation characteristics from theoretical analysis under such an excitation condition. The additional excitation weakens rapidly these electricity generation characteristics, as its excitation frequency goes away from the natural frequency. It is verified that such variations in electricity generation characteristics get closer to the situation of the random excitation from the electricity generation experiment. Then from the estimation based on Q value, the electricity generation efficiency becomes more insensitive against shifts in the additional excitation frequency than the mechanical power and electric power and also becomes insensitive with increases in the plate thickness and excitation force ratio. To improve the electricity generation characteristics by using the acoustic radiation power derived from the plate vibration, a cylinder that has the above plates at both ends is adopted, and the mechanical–acoustic coupling between the plate vibrations and internal sound field is used. However, although the application of the random excitation to this system suppresses the electricity generation characteristics more extremely than those of the harmonic excitation, the characteristics are hardly improved only by mechanical-acoustic coupling.

Keywords: Energy harvesting, Electricity generation system, Piezoelectric element, Harmonic excitation, Random excitation

1. Introduction

Energy harvesting is an energy conversion technology with an output power of μW to mW, or at most a few W, which can be used as a stand-alone power source for small electronic devices[1)]. Generally, it utilizes various energy sources, such as heat, wind, solar energies, and so on. Among the various energy harvesting possibilities being proposed and under consideration for practical application, the energy harvesting technologies based on vibration power generation will become increasingly essential as a power source technology in the future[2,3)], including concepts such as the "Trillion Sensor," which will create a market of 1 trillion sensors per year[4)]. This power generation requires a two-step process: first, the mechanical energy in the environment is captured in the device, and subsequently converted into electrical energy. From a material point of view, there are two types of vibration power generation: magnetostrictive and piezoelectric. In both cases, it is important to model and understand the vibration problem according to the realistic environment, for a better energy conversion efficiency[5)]. The Sustainable Development Goals (SDGs), proposed by the United Nations in 2015[6)] call for improvements in global energy efficiency by 2030, and improvements in the harvesting efficiency by understanding vibration will make a significant contribution to this goal. Especially, untapped vibration energy exists fully around us and technologies to be able to scavenge such an energy are so significant. Although several methods to harvest the vibration energy have been proposed a lot, piezoelectric materials that can convert it into usable electric energy are taken up and electricity generation systems that are attaching the materials

*1 Professor, Department of Prime Mover Engineering
*2 Assistant Professor, Department of Precision Engineering
*3 Junior Associate Professor, Department of Precision Engineering

to host structures attract considerable attention. Because a simple cantilever beam is adopted generally as the host structure, it is comparatively easy to theoretically model it and to carry out the theoretical procedure model[7].

In such an energy-harvesting system, matching the load impedance with the input impedance is significant. Therefore, the variations in the maximum power have been considered by changing the resistance of the resistor by which the load impedance was characterized[8,10]. Then to improve the modal equivalent stiffness ratio, modal electro-mechanical coupling coefficient, and modal piezoelectric voltage coefficient of a piezoelectric element attached to a beam, two mechanical impedance matching methods were proposed, and then they were derived from using spacers between the piezoelectric element and beam structure and from tuning for the size of the piezoelectric element[9]. In the case of the cantilever beam that was selected as the host structure, because the vibration characteristics were adjusted easily due to a tip mass and related directly to the efficiency (with respect to the tip mass), the influence of the size and position on electricity generation characteristics was considered[8]. In general, the rectangular strip shape is adopted as the host structure. However, because it is also possible to assume various shapes, electricity generation characteristics were compared in rectangular and triangular shapes, and it was verified that the performance of a triangular shape was superior to that of a rectangular shape [10].

In this study, a circular plate, on which a piezoelectric element is installed at its center, is adopted as the host structure and is subjected to a harmonic point force. However, to assume the application of this electricity generation system to actual environment, the point force, whose frequency is different from the natural frequency, is also added to the original point force. Then the excitation force ratio, which is determined by dividing the additional point force by the original point force, is defined. The mechanical power supplied to the plate, the electric power in the electricity generation and the electricity generation efficiency derived from those powers are considered as electricity generation characteristics from theoretical analysis under such an excitation condition. On the other hand, to utilize an acoustic radiation derived from the plate vibration for energy-harvesting, a cylinder that has the above plates at both ends is also adopted as the electricity generation system and mechanical-acoustic coupling is caused between the plate vibrations and a sound field into the cylindrical enclosure by subjecting one side of each plate to harmonic or random excitation. Then the effect of coupling is evaluated by comparing with the efficiencies in the electricity generation system of only plate.

2. Analytical method

2.1 *Analytical model*

Fig. 1 shows the analytical model of a plate that is supported by translational and rotational springs. These springs are distributed at constant intervals and the support conditions are determined by the translational spring stiffness T and the rotational spring stiffness R. The plate whose radius and thickness are denoted by r_c and h_c, respectively, have a Young's modulus E_c and a Poisson's ratio ν_c. Piezoelectric element is installed at the center of the plates and have radius r_p, thickness h_p, Young's modulus E_p, and Poisson's ratio ν_p. Then an electrode plate that is made of brass is sandwiched between the above plate and piezoelectric element and has radius r_b, thickness h_b, Young's modulus E_b and Poisson's ratio ν_b. The suffixes c, p and b denote the circular plate, piezoelectric element and electrode plate. The coordinates are radius r and angle θ on the plate and z indicates the direction vertical to its surface. The plate was excited by the periodic point force F at distance r_e and angle θ_e after the $r\theta$ coordinates and its natural frequency was employed as the excitation frequency. However, the excitations combined with other frequency components were also assumed.

The flexural displacement of the plate is denoted by w_c and the displacement of the piezoelectric element installed on the plate is denoted by w_p. Their displacements are expressed by Eq. (1) as suitable trial functions and have the plate mode X^s_{nm} of Eq. (2). w_p is identical to w_c, because it is assumed that the piezoelectric element adheres completely to the plate through the electrode plate.

$$w_c = w_p = \sum_{s=0}^{1}\sum_{n=0}^{\infty}\sum_{m=0}^{\infty} X^s_{nm} A^s_{nm}\left(\mathrm{e}^{\mathrm{j}\omega_1 t} + \mathrm{e}^{\mathrm{j}\omega_2 t} + \cdots + \mathrm{e}^{\mathrm{j}\omega_k t}\right), \qquad k = 1, 2, \cdots, \tag{1}$$

$$X^s_{nm} = \sin(n\theta + s\pi/2)\,(r/r_c)^m, \tag{2}$$

where n and m are the circumferential and radial orders and s is symmetry index with respect to the vibration mode. A^s_{nm} is coefficient to be determined and correspond to the amplitude of the flexural displacement. ω_1 is the angular frequency in the

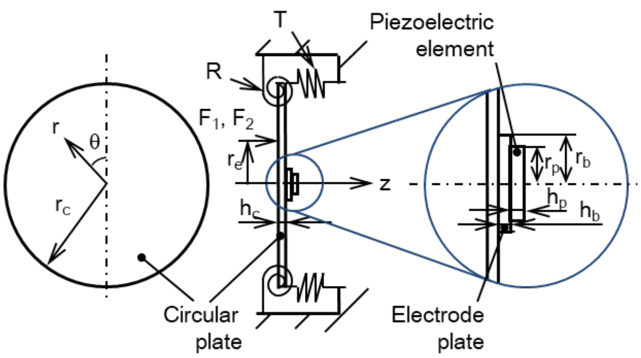

Fig. 1 Configuration of analytical model.

natural mode (0,0), which is denoted by (n,m) mode, and corresponds to the angular frequency of the harmonic point force acting on the plate. Therefore, $\omega_2, \omega_3, \cdots, \omega_k$ correspond to the angular frequencies of point forces added to the harmonic point force and t is the elapsed time.

With respect to the the piezoelectric element on the plate, the electric field E_p, which occurs in the above direction of the piezoelectric element, is expressed as follows:

$$\begin{aligned} E_p &= Y_{nm} v_p = -R_p \dot{q}_p \\ &= \mathrm{j}\omega B_{nm}^s \{ \mathrm{e}^{\mathrm{j}\omega_1 t} + \mathrm{e}^{\mathrm{j}\omega_2 t} + \cdots + \mathrm{e}^{\mathrm{j}\omega_k t} \}. \end{aligned} \tag{3}$$

v_p is the voltage that occurs in the electric field. The electric potential across the piezoelectric element is constant since it is assumed that it does not reach the plate, so that Y_{nm} is defined as Equation (4). R_p is the overall resistance value in an electricity generation circuit. The magnitude of the electric charge q_p depends on the coefficient B_{nm}^s that is determined in this analysis as with A_{nm}^s.

$$Y_{nm} = \begin{cases} -1/h_p, & h_c/2 + h_b < z < h_c/2 + h_b + h_p, \\ 0, & -h_c/2 < z < h_c/2 + h_b, \end{cases} \tag{4}$$

$$q_p = B_{nm}^s \{ \mathrm{e}^{\mathrm{j}\omega_1 t} + \mathrm{e}^{\mathrm{j}\omega_2 t} + \cdots + \mathrm{e}^{\mathrm{j}\omega_k t} \}. \tag{5}$$

To consider electro-mechanical coupling between the plate and piezoelectric element, the elements $M_{nmm'}^s$ and $K_{nmm'}^s$ of the mass and stiffness matrices can be defined as

$$M_{pnmm'}^s = \int_{V_p} \rho_p X_{nm}^s X_{nm'}^s \mathrm{d}V_p, \tag{6}$$

$$K_{pnmm'}^s = \int_{V_p} z^2 X_{nm}^{s\,''} E_p^E X_{nm'}^{s\,''} \mathrm{d}V_p. \tag{7}$$

The index m' has a transposed relation to a radial order m, then ρ_p and V_p denote the density and volume of the piezoelectric element, respectively. The respective elements of electro-mechanical coupling and capacitance matrices are denoted by β and C_p and they are defined as follows:

$$\beta = -\int_{V_p} z \rho_p X_{nm}^s e Y_{nm'} \mathrm{d}V_p, \tag{8}$$

$$C_p = \int_{V_p} Y_{nm} \gamma^\varepsilon Y_{nm'} \mathrm{d}V_p, \tag{9}$$

$$e = d_{31} E_P^E, \tag{10}$$

e is the piezoelectric coupling coefficient that includes the piezoelectric strain constant d_{31}, as described in Equation (10) and γ^ε indicates the dielectric constant when a strain is constant.

2.2 *Governing equations of electro-mechanical coupling*

To formulate the plate motion, Hamilton's principle is applied to the analytical model:

$$\delta H = \delta \int_{t_0}^{t_1} \left(T_c + T_p + T_b - U_c - U_p - U_b - U_s + W \right) \mathrm{d}t = 0, \tag{11}$$

where H is the Hamiltonian; T_c, T_p and T_b are the kinetic energy of the circular plate, piezoelectric element and electrode plate, respectively; and U_c, U_p and U_b are their respective potential energies. U_s is the elastic energy stored in the springs, and W is the total work done on the plate by the point force. Finally, t_0 and t_1 are two arbitrary times. On the other hand, if the first variation is carried out in terms of the piezoelectric part on the plate, we can obtain

$$\begin{aligned} \delta \int_{t_0}^{t_1} (T_p - U_p) \mathrm{d}t = \frac{1}{2} \int_{t_0}^{t_1} \int_{V_p} \{ \rho_p \dot{w}_p \delta \dot{w}_p \\ -(E_p^E \varepsilon_p - e E_p) \delta \varepsilon_p + (e \varepsilon_p + \gamma^\varepsilon E_p) \delta E_p \} V_p \mathrm{d}t, \end{aligned} \tag{12}$$

where $\dot{w}_p$ is the vibration velocity of the piezoelectric element on the plate and ε_p is the in-plane strain within that element.

Here, the governing equation of electro-mechanical coupling with respect to the system is determined. This equation defines the mechanical motion and electrical characteristics of this coupling system. The motion equation of the plate was obtained by applying the flexural displacement w_c of Eq. (1) to the Hamiltonian H of Eq. (11) in the same manner as Eq. (12) of the piezoelectric part. Then the motion of the plate having a piezoelectric part, which generates electricity by the plate vibration, is governed by the following Eq. (13):

$$\begin{aligned} &\sum_{m'=0}^{\infty} \langle [K_{cnmm'}^s (1 + j\eta_c) + K_{pnmm'}^s (1 + j\eta_p) + K_{bnmm'}^s \times \\ &K_{bnmm'}^s (1 + j\eta_b) + r_c F_{sn} \left\{ T + \left(\frac{m}{r_c} \right) \left(\frac{m'}{r_c} \right) R \right\}] \{ e^{j(\omega_1 t + \alpha_1)} + \\ &e^{j(\omega_2 t + \alpha_2)} + \cdots + e^{j(\omega_k t + \alpha_k)} \} - (M_{cnmm'}^s + M_{pnmm'}^s + \\ &M_{bnmm'}^s) \{ {\omega_1}^2 e^{j(\omega_1 t + \alpha_1)} + {\omega_2}^2 e^{j(\omega_2 t + \alpha_2)} + \cdots + \\ &{\omega_k}^2 e^{j(\omega_k t + \alpha_k)} \} \rangle A_{nm'}^s - \sum_{m'=0}^{\infty} \beta v_p B_{nm'}^s \{ e^{j(\omega_1 t + \alpha_1)} + \\ &e^{j(\omega_2 t + \alpha_2)} + \cdots + e^{j(\omega_k t + \alpha_k)} \} \\ &= \mathbf{F}_{nm}^s \{ e^{j(\omega_1 t + \alpha_1)} + e^{j(\omega_2 t + \alpha_2)} + \cdots + e^{j(\omega_k t + \alpha_k)} \}. \end{aligned} \tag{13}$$

$K_{cnmm'}^s$ and $K_{bnmm'}^s$ are stiffness matrix elements of the structural and electrode plates, respectively. $M_{cnmm'}^s$ and $M_{bnmm'}^s$ are also mass matrix elements of the respective parts. These are elements of the symmetrical matrices, since the index m' has a transposed relation to m, as with $M_{pnmm'}^s$ and $K_{pnmm'}^s$. η_c, η_p and η_b signify the structural damping factors of the end plate, piezoelectric element and electrode plate, respectively. Then F_{sn} is a coefficient that is determined by the indices n and s and $\mathbf{F}_{nm}^s$ is a load vector that is applied to the plate as the point force. The details of the coefficient F_{sn} and the element F_{nm}^s of the vector are as follows:

$$F_{sn}=\begin{cases}\pi, \text{at } n\neq 0,\\ 0, \text{at } n=0 \text{ and } s=0,\\ 2\pi, \text{at } n=0 \text{ and } s=1,\end{cases} \tag{14}$$

$$F_{nm}^{s}=\int_{A_c} F\delta(r-r_e)\delta(\theta-\theta_e)X_{nm}^{s}dA_c. \tag{15}$$

Here, the point force is expressed by performing Eq. (15) including the delta function δ on the plate, whose area is denoted by A_c.

On the other hand, the electricity generation behavior of the piezoelectric element is also governed by the following Equations (16):

$$\sum_{m'=0}^{\infty} C_p^{-1}\beta A_{nm'}^{s}=\sum_{m'=0}^{\infty}\left(j\omega R_p+C_p^{-1}\right)B_{nm'}^{s}. \tag{16}$$

The relationship between A_{nm}^{s} and B_{nm}^{s} is applied to Eq. (13) and these coefficients can be derived by solving the above simultaneous equations. However, if the plate is excited by the point force of its natural frequency and the behavior is assumed to be harmonic, $e^{j\omega t}$ could be eliminated in Eq. (13).

Since the flexural displacement w_c is calculated by substituting A_{nm}^{s} for Eq. (1), the vibration velocity $\dot{w}_c$ is derived from the following equation:

$$\dot{w}_c=j\omega\sum_{s=0}^{1}\sum_{n=0}^{\infty}\sum_{m=0}^{\infty}X_{nm}^{s}A_{nm}^{s}e^{j\omega t}. \tag{17}$$

The mechanical power P_m supplied to the plate is obtained from the time history data of the products of the vibration velocity and the force at the excited point. The voltage v_p is calculated by substituting B_{nm}^{s} for Equations (3) and (5), when the piezoelectric element generates electricity by the plate vibration. Then the electric power P_e is also obtained from the time history data of the products of its voltage v_p and the electric current corresponding to v_p.

3. Experimental apparatus and method

In the experimental study, a circular aluminum plate was employed and was sandwiched between two flanges fastened by bolts to emulate the analytical model, as shown in Fig. 2(a). The flanges have a short steel cylinder, respectively, to fix the plate on their end faces. Although the cylinder on the excitation side is very short not to prevent the installation of a small vibrator and is similar to a ring, another cylinder have somewhat longer length to disturb an inflow of the acoustic radiation from the excitation side. The plate had the radius r_c of 153 mm and the thickness h_c was changed as in 2.0, 2.5, 3.0 and 4.0 mm. The point force was applied to the plate by the small vibrator, the amplitude F was set to 1 N. The excitation was carried out not only near the natural frequency of the (0,0) mode but also by a random wave. Then the position of the point force r_e was 61 mm and was set to $r_e/r_c = 0.4$ by means of normalizing by radius r_c.

The point force F was measured by the load cell embedded with the excitation stick, which was short as much as possible between the plate and load cell to avoid the influence of its additional mass. The acceleration a_e was measured by the acceleration sensor that was installed in close proximity of the excitation position. Because F and a_e were time history data, the vibration velocity $\dot{w}_c$ was calculated from a_e. The mechanical power P_m supplied to the plate by the small vibrator was estimated from the relationship between F and $\dot{w}_c$.

The piezoelectric element used to perform the electricity generation experiment was comprised of a circular piezoelectric part constructed of ceramics and a circular electrode part constructed of brass. The piezoelectric and ceramics parts had radiuses r_p and r_b of 12.5 and 17.5 mm and thicknesses h_p and h_b of 0.23 and 0.30 mm, respectively. The piezoelectric element was installed at the center of the plate as with the analytical model. The voltage v_p, which was generated with the expansion and contraction of the piezoelectric element on the plate surface derived from the flexural vibration of the plate, was measured by FFT analyzer and was also time history data.

The piezoelectric element was incorporated in the resistance circuit, which was composed of three resistors having resistances R_v, R_i, and R_c. R_v and R_i are the resistances of the voltmeter and ammeter, which are incorporated into the power meter 9, and were 2 MΩ and 2 mΩ, respectively. However, R_c is the resistance of the resistor to consume the generated electric power and was mainly 97.5 kΩ, and then the resistor was connected outside the power meter. Because the piezoelectric element is assumed to be incorporated in the electrical circuit of the energy-harvesting device and to be connected in series with the resistance for power consumption, it is natural that an electrical current is in-phase to the voltage.

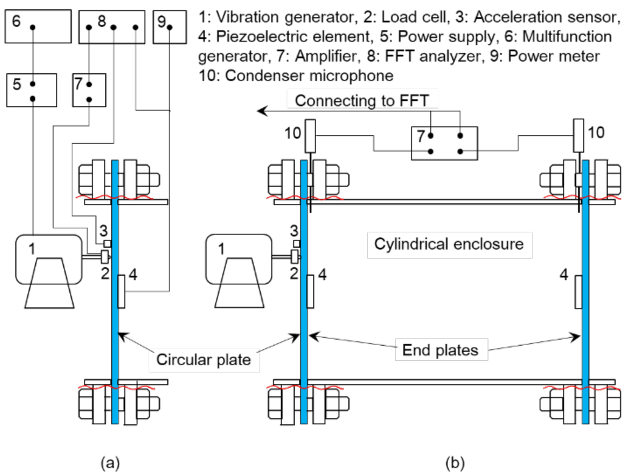

Fig. 2 Configuration of experimental apparatus: (a) without cylinder and (b) with cylinder.

Therefore, the electric power P_e was proportional to the square of v_p and could be obtained from only the voltage because of Ohm's law. Just in case, P_e was also measured by the power meter as well.

To utilize an acoustic energy radiated from the plate because of the improvement of the electricity generation performance, a steel cylinder and the same plate were added in the above electricity generation system and this was constructed of three systems, which were the excited plate, cylindrical enclosure and non-excited plate, as shown in Fig. 2(b). The application of mechanical-acoustic coupling, which is caused between the plate vibrations and an internal sound field into the cylindrical enclosure by subjecting one side of each plate to a harmonic point force, is expected to the improvement of the electricity generation performance. The coupling situation was grasped from the estimation of the internal acoustic characteristics, which was involved directly in coupling. Therefore, although the sound pressure level in the cavity was measured using condenser microphones, a probe tube was attached to each microphone not to prevent the sound wave propagation inside the cavity. Because the sound pressure level is maximized near both end plates when the sound field becomes resonant, the tips of the probe tubes were located near the plates and the cylinder wall. The measuring items except the sound pressure level were carried out in the same manner as those of the electricity generation experiment of only the plate.

4. Results and discussion

4.1 *Influence of plate thickness and support condition electricity generation characteristics*

The plate and piezoelectric element were the same as the experimental apparatus in the respective dimensions, and had the mechanical and electrical properties shown in Table 1. The plate radii r_c were constant at 153 mm, and the plate thickness h_c ranged from 1.0 to 10 mm. The analysis herein was based on the assumption of a thin circular plate, specifically, the stress was assumed as the plane stress field, so that the stress was not considered in the direction normal to the plane. Therefore, because the stress was increased relatively in the plate thickness direction with increasing h_c, it was supposed that the deviation between the analytical and actual situations might be expanded as h_c increased. However, since it was difficult to specify the range in which the circular plate could be regarded as a thin-walled plate, h_c was set to the above range in order to cover the range of the thin-walled.

Table 1 Mechanical and electrical properties.

	Density [kg/m³]	Young's modulus [GPa]	Poisson's ratio
Aluminum plate	2680	70.6	0.33
Electrode plate	6900	100	0.35
Piezoelectric material	8400	132	0.30
	γ^{ε} = 2.213 × 10^{-9} [F/m], d_{31} = -3.7 × 10^{-12} [m/V]		

The support conditions of the plates, which had flexural rigidity D [= $Eh_c^3/\{12(1-\nu^2)\}$], were expressed by the nondimensional stiffness parameters T_n (= $Tr_c{}^3/D$) and R_n (= Rr_c/D). If R_n ranged from 0 to $10^{8.0}$ when T_n was $10^{8.0}$, the support condition could be assumed from a simple support to a clamped support. The plate was subjected to the point force F_e that was set to 1 N and was located at r_e/r_c = 0.4, as with the excitation experiment.

Fig. 3(a) and (b) show the mechanical power P_m supplied to the plate by the small vibrator and the electric power P_e, which are regarded as electricity generation characteristics, as functions of the plate thickness h_c with changing R_n. Both of P_m and P_e are maximized at h_c = 1.0 mm and decrease rapidly with increasing h_c. When R_n increases from $10^{1.0}$, the flexural displacement is suppressed due to reinforcing the rigidity of the whole structure, as the result that P_m and P_e have a decreasing trend. Although these have the similar tendency, the relative tendency to decrease P_e with increasing h_c is somewhat extreme in comparison with that of P_m. Here, when the plate, whose R_n is 0 and $10^{8.0}$, is subjected to a point force at the plate center, the flexural displacement and bending stress are considered in the statics. The flexural displacement

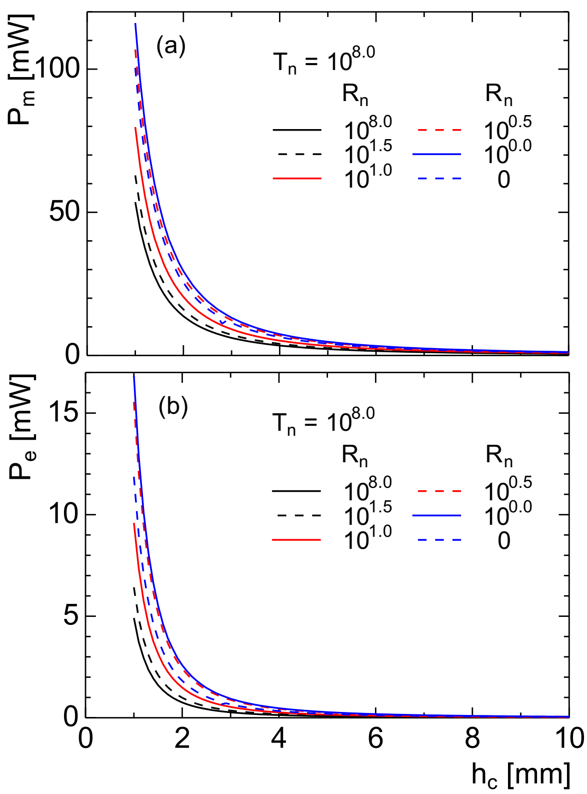

Fig. 3 Variations in (a) mechanical power and (b) electric power with changing plate thickness.

at the center is denoted by w_{sm} and w_{cm}, which are derived from R_n = 0 and $10^{8.0}$, respectively, and then the bending stress at the center is denoted by σ_{sm} and σ_{cm}. These flexural displacement and bending stress can be calculated as follows:

$$w_{sm} = \frac{3+\nu_c}{1+\nu_c}\frac{Fr_c^2}{16\pi D}, \tag{18}$$

$$w_{cm} = \frac{Fr_c^2}{16\pi D}, \tag{19}$$

$$\sigma_{sm} = \frac{F}{h_c^2}\left\{0.477 + (1+\nu_c)\left(0.485\ln\frac{r_c}{h_c} + 0.52\right)\right\}, \tag{20}$$

$$\sigma_{cm} = \frac{F}{h_c^2}(1+\nu_c)\left(0.485\ln\frac{r_c}{h_c} + 0.52\right). \tag{21}$$

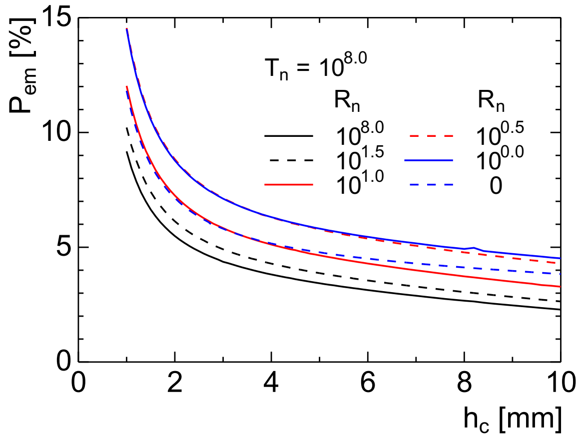

Fig. 4 Electricity generation efficiency as function of plate thickness with changing rotational stiffness.

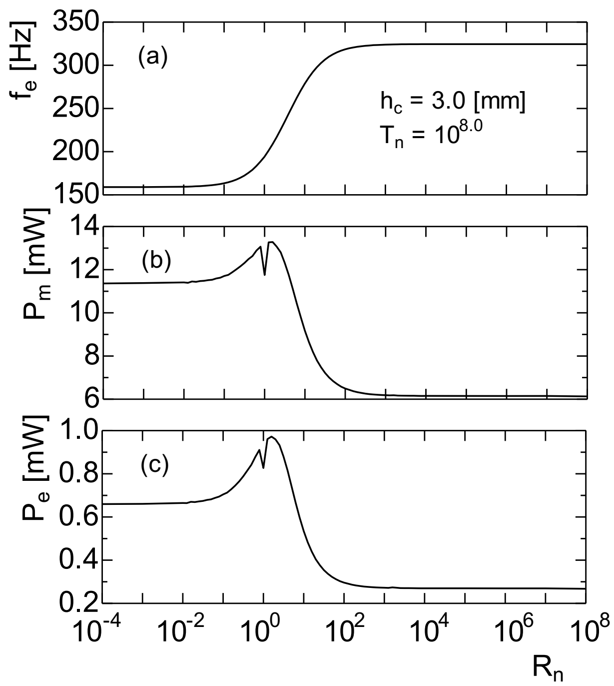

Fig. 5 Variations in (a) natural frequency, (b) mechanical power and (c) electric power with changing rotational stiffness.

P_m depends on w_{sm} and w_{cm}, having been obtained from the product F and $\dot{w}_c$. According to Eqs. (18) and (19), a decrease rate w_{cm}/w_{sm} is constant despite of changes in h_c, so that the rate of decrease in P_m is also maintained at the constant ratio. On the other hand, P_e depends on σ_{sm} and σ_{cm}, having been involved directly with the in-plane strain. The decrease rate σ_{cm}/σ_{sm} decreases with increasing h_c, being calculated actually based on Eqs. (20) and (21). In other words, the rate of decrease in P_e increases with h_c. In view of these situations, it is possible to explain a slight difference between variations in P_m and P_e with changing h_c.

In addition, to consider this relationship between P_m and P_e, the electricity generation efficiency P_{em} is defined as follows:

$$P_{em} = \frac{P_e}{P_m} \times 100\ [\%]. \tag{22}$$

Because P_{em} that corresponds to above P_m and P_e is indicated in Fig. 4, which has the same manner as Fig. 3, it is natural that P_{em} behaves in tendency similar to the above powers. However, P_{em} suppresses considerably the variation rate with h_c in comparison with those of P_m and P_e and is clearly different with changing R_n in the whole range of h_c. P_{em} decreased with increasing R_n as with P_m and P_e, whereas those did not obey that decrease trend, so that the influence of R_n on electricity generation characteristics is considered in some detail.

Here, the plate of h_c = 3.0 mm is taken up and not only P_m and P_e but also its natural frequency f_e attract attention with changing R_n in Fig. 5. f_e is around 160 Hz and is almost constant up to the vicinity of $R_n = 10^{-0.5}$ from R_n = 0, which is identical to the simple support and is not exhibited in Fig. 5(a). f_e increases until around 320 Hz with increasing R_n after that and is maintained up to $R_n = 10^{8.0}$. P_m is around 11.5 mW and is almost constant up to the vicinity of $R_n = 10^{-0.5}$ when R_n increases, as shown in Fig. 5(b). After that, P_m increases with R_n and is maximized (13.3 mW) around $R_n = 10^{0.2}$. Then P_m turns to decreases and reaches around 6.15 mW, and then it is maintained up to $R_n = 10^{8.0}$. We can make sure that P_e has the behavior similar to P_m from Fig. 5(c) and P_m and P_e behave in a quite different manner from f_e.

4.2 *Influence of additional force on electricity generation characteristics*

In the previous section, F_e that was derived from the natural frequency f_e was regarded as the excitation force. Here, a new situation, in which another excitation force F_a is added to F_e, is assumed and the excitation frequency of F_a is denoted by f_a, and then F_a/F_e is regarded as the excitation force ratio that is denoted by F_R. In this case, $T_n = 10^{8.0}$ and $R_n = 10^{1.0}$ are adopted to get closer to the experimental support conditio Fig. 6 shows the mechanical power P_m as functions of f_a when

F_R =1.0 and h_c = 2.0, 3.0 and 4.0 mm. P_m reaches the respective peaks when f_a is identical to f_e and the peak values decrease in order of h_c = 2.0, 3.0 and 4.0 mm as with Fig. 3(a). However, P_m decreases rapidly due to separating f_a from f_e no matter what h_c is.

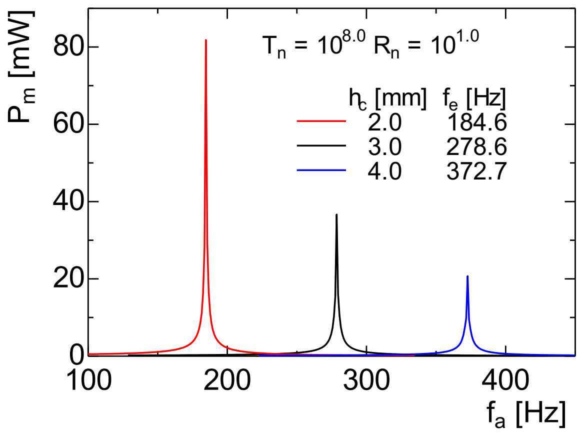

Fig. 6 Mechanical power as function of additional excitation frequency with changing plate thickness.

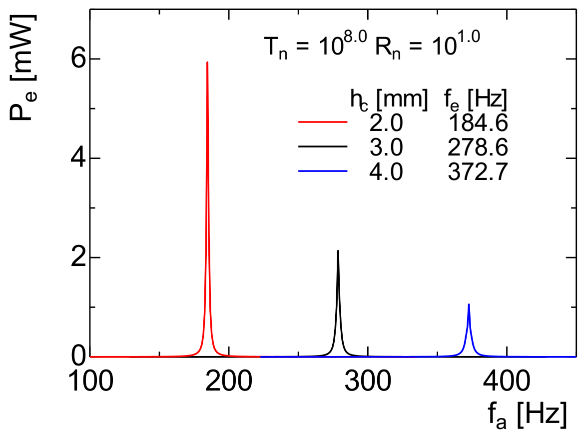

Fig. 7 Electric power as function of additional excitation frequency with changing plate thickness.

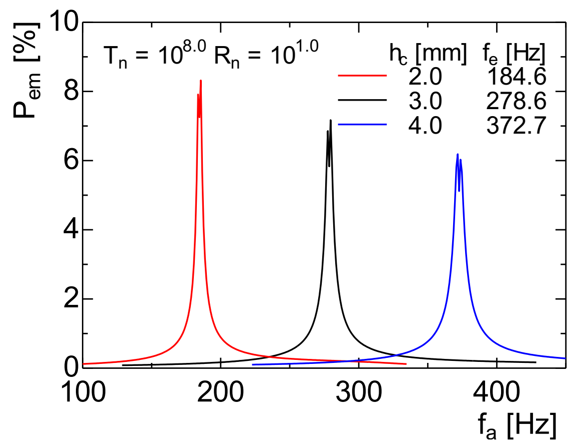

Fig. 8 Electricity generation efficiency as function of additional excitation frequency with changing plate thickness.

P_e is also indicated in Fig. 7, which is shown in the same manner as Fig. 6, and tends to vary similarly to P_m. However, the rate of decrease in P_e is greater than that of P_m and this is because P_m and P_e were involved with the flexural displacement and bending stress, respectively, as explained in Eqs. (18) – (21). Specifically, we can make sure of the following relationships by taking notice of Eqs. (19) and (21) based on the clamped support. The rate of variation in the flexural displacement is proportional to the cube of plate thickness ratio and the bending stress is less in the variation rate with the plate thickness ratio than the flexural displacement. However, by taking into consideration the strain energy, which is proportional to the square of bending stress, it is valid that P_m and P_e have the above decreasing trend with increasing h_c. Then Fig. 8 shows the electricity generation efficiency P_{em}, which was calculated from P_m and P_e, as functions of the excitation frequency f_a of the additional point force F_a. The rate of variation in P_{em} with h_c is moderated in

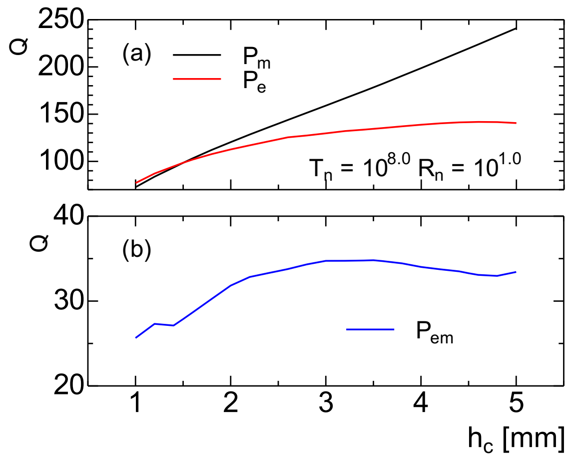

Fig. 9 Variations in Q values with changing plate thickness: (a) mechanical and electric powers and (b) electricity generation efficiency.

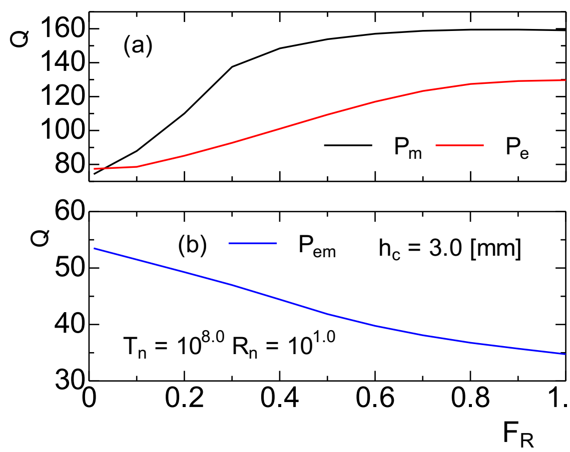

Fig. 10 Variations in Q values with changing excitation force ratio: (a) mechanical and electric powers and (b) electricity generation efficiency.

comparison with those of P_m and P_e which were relatively close, because P_{em} was obtained from dividing P_e by P_m. In order to consider not only the respective values but also generation situations of the respective peaks, Q value was adopted and was defined as follows:

$$Q = \frac{f_e}{f_2 - f_1}, \tag{23}$$

where f_2 - f_1 is half-value width with respect to the respective peaks in Figs. 6 – 8.

Fig. 9 shows such a Q value as functions of h_c on condition that P_m and P_e (Fig. (a)) and P_{em} (Fig. (b)) are indicated by means of separating figures, because Q in P_m and P_e is greater and varies in the more extensive range than that of P_{em}. In general, Q value is a dimensionless quantity to express a state of vibration system and is the quantity dividing energy stored in the vibration system by energy dissipated from the system in a period. In other words, this value is also index to express the sharpness of peaks and such a function was utilized here. Although the natural frequency f_e was proportional to h_c, since Q in P_m also increases linearly with h_c, it may look like promoting the sharpness of P_m with increasing h_c. Although the variation rate f_e / h_c was around 94.0, Q / h_c is around 42.1. In order to make Q behave like f_e, Q / h_c needs to be increased up to around 73.5, and that value is based on the assumption that the half width at h_c = 1.0 mm is maintained in the whole range of h_c. However, because Q / h_c is much smaller than not only f_e / h_c but also 73.5, actually, the sharpness of P_m peaks becomes dull gradually with increasing h_c.

Although Q in P_e increases with h_c as with that in P_m, its increase rate decreases gradually with increasing h_c. In other words, the sharpness of P_e peaks becomes dull more rapidly with increasing h_c. On the other hand, Q in P_{em} ranges from 25 to 35 and distributes in the lower range than those in P_m and P_e, so that the sharpness of P_{em} peaks becomes duller than that of P_m and P_e peaks. Then changes in Q of P_{em} are suppressed in comparison with those of other cases, in particular, its Q turns to a decreasing trend beyond h_c = 3.5 mm and the situation to dull the sharpness of P_{em} peaks is promoted more strongly. The tendencies mentioned above correspond to variation tendencies of the peaks in Figs. 6 – 8.

Up to here, the original point force F_e was coincident with the additional point force F_a, i.e., the excitation force ratio F_R that is 1.0 was regard as the analysis condition. Therefore, shifts in Q values with respect to P_m, P_e and P_{em} herein were considered when h_c = 3.0 mm and the F_R range of 0.01 to 1.0. Q in P_m and P_e is shown in Fig. 10(a) and Q in P_{em} is shown in Fig. 10(b). In these cases, since f_e is set to 278.6 Hz and is constant, the consideration against changes in f_e, which was taken in Figs. 6 – 8, is ignored. Although Q in P_m increases greatly with F_R up to $F_R \simeq 0.35$, its increase is weakened after that and it converges to the vicinity of 159. Also increasing with F_R, Q in P_e is smaller than that of P_m and behaves more monotonously.

Q in P_{em} decreases gradually with increasing F_R and presents a totally reverse tendency against those in P_m and P_e. This takes place in the lower range of Q as well as that of changes in h_c, so that the peaks of P_{em} become duller with increases in h_c and F_R than those of P_m and P_e. In other words, it is suggested that P_{em} becomes more insensitive with increases in additional forces than P_m and P_e.

4.3 *Electricity generation efficiency for random excitation*

In previous section, the electricity generation characteristics attracted attention on condition that the plate was subjected to two point forces, whose frequencies were different. Considering the actual vibration environment, we want to aim to apply random excitation to this electricity generation system. However, the application of the random excitation to the analytical model was hard in reason why our computer performance lacked in calculation capacity and speed. Therefore, the electricity generation efficiency P_{em} under the random excitation was estimated from the experimental results.

P_{em} that was obtained from the electricity generation experiment in Fig. 2(a) is indicated with changes in the plate thickness h_c by black circle and line in Fig. 11(a). P_{em} decreases with increasing h_c and has the tendency similar to theoretical value of $T_n = 10^{8.0}$ and $R_n = 10^{1.0}$ in Fig. 4, being smaller than theoretical value that did not take into consideration the acoustic radiation derived from the plate vibration. Then a part energy of such an acoustic radiation can be scavenged by causing air column resonance within a cavity. Specifically, mechanical-acoustic coupling is caused not only between the plate vibration on the excitation side and the internal acoustic field but also between the plate vibration on the non-excitation side and the internal acoustic field, as shown in Fig. 2(b). In actual experiment, the end plates of the same thicknesses were chosen and then cylinder length L at which coupling is promoted was set. Such a P_{em} is drawn by red circle and line in Fig. 11(a) and presents a totally reverse tendency against the above results without the cavity, as the result that we can confirm the improvement of electricity generation characteristics by means of coupling.

The results based on applying the random excitation to the plate of Fig. 2(a) are shown by blue circle and line in Fig. 11(b). Although P_{em} of the random excitation decreases gradually with increasing h_c and has the behavior similar to that of the excitation by the natural frequency, its values are suppressed more extremely than those of the excitation by the natural frequency. However, when h_c = 3.0 mm in Fig. 8, if it

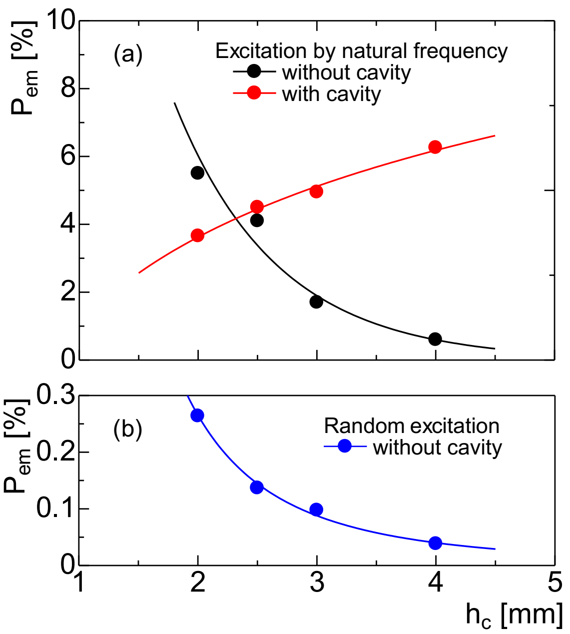

Fig. 11 Variations in electricity generation efficiency with changing plate thickness: (a) harmonic excitation and (b) random excitation.

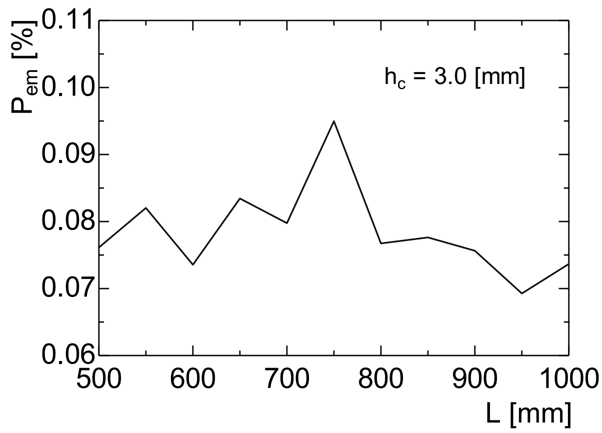

Fig. 12 Electricity generation efficiency as functions of cylinder length under random excitation.

is considered that P_{em} was 8.19 $\times 10^{-2}$ and 0.167 % at f_a = 128.6 and 428.6 Hz, which are the upper and lower limits in the analytical frequency range of f_a, respectively, it is realized that these experimental results are valid. In other words, the additional excitation, whose frequency goes away from the natural frequency, gets closer rapidly to the situation of the random excitation. The random excitation was applied to the experimental apparatus of h_c = 3.0 mm with the cavity in Fig. 2(b) and its P_{em} is shown with changes in the cylinder length L in Fig. 12. However, the coupling effect that was exhibited in Fig. 11(a) is not verified from this result, so that a new method to improve electricity generation characteristics needs to be attempted.

5. Conclusion

In this study, an electricity generation system, which consisted of a circular plate with a piezoelectric element installed at its center, was examined. The plate was subjected to the point force of the natural frequency, which was derived from the plate material, dimensions and support condition, in the case of the original application. To assume the application of this electricity generation system to actual environment, the point force, whose frequency was different from the natural frequency, was added to the original point force. Then the excitation force ratio, which was determined by dividing the additional point force by the original point force, was defined. The mechanical power supplied to the plate, the electric power in the electricity generation and the electricity generation efficiency derived from those powers were considered as electricity generation characteristics from theoretical analysis under such an excitation condition. As a result, the respective values of electricity generation characteristics decreased rapidly with changes in the additional excitation frequency that went away from the natural frequency. Then it was verified that such an additional excitation got closer to the situation of the random excitation from the electricity generation experiment, and then from the estimation based on Q value, the electricity generation efficiency became more insensitive against shifts in the additional excitation frequency than the above two powers and also became insensitive with increases in the plate thickness and excitation force ratio.

To improve the electricity generation characteristics by using the acoustic radiation power derived from the plate vibration, a cylinder that had the above plates at both ends was adopted, and the mechanical–acoustic coupling between the plate vibrations and internal sound field was used. In the case of the excitation by the natural frequency, the improvement of the electricity generation efficiency by coupling was promoted with increasing the plate thickness. However, although the application of the random excitation to this system suppressed the electricity generation characteristics more extremely than those of the harmonic excitation, the characteristics were hardly improved only by mechanical-acoustic coupling.

References

1) M. Loreto, et al.: *Handbook of Energy Harvesting Power Supplies and Applications* (CRC Press), ISBN: 9814303062.

2) T. Ueno: Performance of Improved Magnetostrictive Vibrational Power Generator, Simple and High Power Output for Practical Applications, J. Appl. Phys **117**, 17A740 (2015).

3) M. Umeda, et al: Self-Generation Door Alarm System using Impact Induced Piezoelectric Vibration, Trans. Inst. Electr. Eng. Jpn. Sect. E **123**, 534 (2003) (in Japanese).

4) S. Kaminaga and S. Kanao: Advent of Trillion Sensors (TSensors) and the Forthcoming Challenges, J. Inst. Electr. Eng. Jpn. **135**, 91 (2015).

5) A. Erturk and D.J. Inman: *Piezoelectric Energy Harvesting* (Wiley), ISBN: 9814303062.

6) United Nations: *Resolution adopted by the General Assembly on 25 September 2015, Transforming our world*, the *2030 Agenda for Sustainable Development*, (2015), A/ RES/ 70/1.

7) S.R. Anton and H.A. Sodano: A Review of Power Harvesting Using Piezoelectric Materials, Smart Materials and Structures **16** (2007) No. 3, 1 (2003–2006).

8) W.G. Ali and S.W. Ibrahim: Power Analysis for Piezoelectric Energy Harvester, Energy and Power Engineering **4**, 496 (2012).

9) K. Yamada, H. Matsuhira and H. Utsuno: Improvement of Efficiency of Piezoelectric Element Attached to Beam Based on Mechanical Impedance Matching, J. Sound Vib. **333** No. 1, 52 (2014).

10) A.A. Basari, et al.: Shape Effect of Piezoelectric Energy Harvester on Vibration Power Generation, Journal of Power and Energy Engineering **2**, 117 (2014).

Proc. Schl. Eng. Tokai Univ., Ser. E
46 (2021) 37-42
DOI: 10.18995/24343641.46.37

Performance Improvement of Gasoline Engine Using Linear Actuator: Fundamental Consideration of Heat Effect on Thrust Characteristics

by

Yuhei MAJIMA[*1], Junpei KURODA[*1], Ryo SUZUKI[*1],
Takayoshi NARITA[*2] and Hideaki KATO[*3]

(Received on Apr. 13, 2021 and accepted on Jul. 16, 2021)

Abstract

In order to improve the performance of gasoline engines, a new system that controls the intake and exhaust valves using a linear motor composed of a permanent magnet and a coil has been proposed. In our research group, a simple and lightweight structure with only a coil as the mover of the linear motor was adopted for the purpose of increasing the engine speed. Furthermore, in actual operating conditions, the heat generated in the combustion chamber would transmit to the actuator. That would adversely affect the thrust performance of the actuator. To solve this problem, this study investigated the heat characteristics for the thrust of the linear motor which consists of rare earth magnets by electromagnetic field analysis using the finite element method. From the analysis results, it was found that the proposed actuator can generate a constant thrust force against the position of the valve. Furthermore, by changing the material of the permanent magnet to a samarium-cobalt magnet, the actuator was able to generate a high thrust force even when the actuator heated at a high temperature.

Keywords: Linear motor, Electromagnetic drive valve, Spark-ignition engine, Variable valve system

1. Introduction

In recent years, the development of control technology has led to the advancement of systems in assisting automobile drivers and automatic driving systems [1-3]. Antilock braking systems (ABS), traction control systems (TCS), and electronic brake-force distribution (EBD) are safety features that assist drivers and are installed in many present-day vehicles.

Although such automatic driving and driver assistance systems facilitate driving, they also increase the weight of the vehicle because of devices, such as control devices, used to build the systems. In addition, the number of vehicles equipped with internal combustion engines is expected to continue increasing until 2040, and the demand for high-power engines will increase [4]. Therefore, it is essential to increase the power output of the engine to maintain the same acceleration performance as conventional vehicles.

There are three conditions for increasing the power output of an engine. These conditions include improvements in the filling efficiency and volumetric efficiency of the combustion chamber, rapid combustion, and reduction in friction loss [5]. Various techniques have been developed to address these three issues. Examples include the technology to generate longitudinal vortex flow (tumble flow) in the combustion chamber by forming the shape of the intake pipe and port to achieve rapid combustion. The order is the VTEC system, which switches the lift and timing of the valves at low and high speeds using two different cam profiles [6]. However, the effect of these methods is definite because these methods do not effectively drive the entire operational rotation speed.

There has been research on driving an engine valve by mounting a linear motor on a cylinder head[7, 8]. This

*1 Graduate Student, Course of Mechanical Engineering
*2 Assistant Professor, Department of Prime Mover Engineering
*3 Junior Associate Professor, Department of Prime Mover Engineering

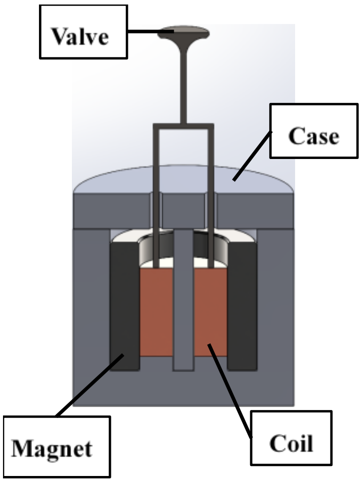

Fig. 1 Electromagnetic-driven valve.

system enables precise changes in the open/close timing and the lift of intake and exhaust valves at each rotation speed during the engine operation to produce a high-power engine.

When the engine operates at a high load, the intake and exhaust valves in the combustion chamber are exposed to high temperatures. In particular, the temperature of the exhaust valve exceeds 600 °C [9)]. The magnets and coils used in the electromagnetic-driven valve are subjected to heat load, owing to heat conduction from the intake and exhaust valves, possibly increasing the electrical resistance of the coils and causing the thermal demagnetization of the magnets. These phenomena adversely affect the thrust of the linear motor in an electromagnetic-driven valve system (EDVS).

To avoid demagnetization of a permanent magnet in an actuator owing to the heat, Okada et al. proposed an actuator that has a seesaw-type mover, solenoid, and no permanent magnet to drive the rocker arm[10)]. Furthermore, to reduce steady current, they proposed to install a permanent magnet in the stator where is far from the combustion chamber to generate a bias magnetic field. However, this actuator was not able to drive at high rotational speed due to the large inertia of the mover. Although Okazaki et al. proposed a small actuator that uses electromagnets to directly drive the mover including the valve[11)], this actuator could only generate a small thrust. That leads to problems, which prevent high rotational speed, with the low valve lift and the longer opening/closing time of the valve.

EDVS that can drive even at high rotational speed, we have investigated a linear actuator with high thrust[12)]. We aim to generate high thrust with the install of a permanent magnet made of rare earth which has a strong flux density and a simple structure of mover that consists of the solenoid[13)].

In this study, as a fundamental study on the thrust characteristics of the proposed actuator, we constructed a finite element analysis model to suppress magnetic saturation and conducted an electromagnetic analysis, considering the operational temperature. Although the size of the actuator was very large to be installed on the cylinder head, we evaluated the effect of heat on the thrust characteristics as the first step. Based on the results, we evaluated the thrust characteristics by changing the materials of the permanent magnet in the linear motor.

2. EDVS

2.1 *EDVS*

A schematic of the EDVS is shown in Fig. 1. The EDVS contained a linear motor consisting of coils and magnets for generating Lorentz force to operate the connected engine valves. The solenoid-driven valve is a fundamental solution to valve surging, jumping, and bouncing in conventional spring-based valve systems. In addition, the amount of variable valve lift and timing in conventional systems is minimal. The proposed EDVS can be used to achieve a wide range of variable valve lifts and valve timings without steps. Moreover, the power output can be expected to exceed those of engines equipped with conventional variable-valve mechanisms. Furthermore, the airflow can be controlled without a throttle valve, and the intake air resistance can be eliminated by the throttle valve. The characteristics mentioned above also make it possible to reduce the weight by eliminating the need for parts, such as camshafts and throttle valves.

Solenoid valves are designed by automobile manufacturers, such as GM and Honda Motor [14,15)]. In addition, valve control using an electromagnetic motor is highly feasible because its operation has been confirmed in a motorcycle engine by Okazaki et al [16)].

2.2 *Linear motor for EDVS*

The finite element model of the linear motor investigated in this study is shown in Fig. 2. The mover was composed of coils and valves. The stator consisted of an inside permanent magnet, an outside permanent magnet, and a case. We applied an electric current to the coil sandwiched between the inside and outside permanent magnets to generate the Lorentz force and achieve thrust. The dimensions of the model are shown in Table 1.

The shape of the case was thickened to prevent

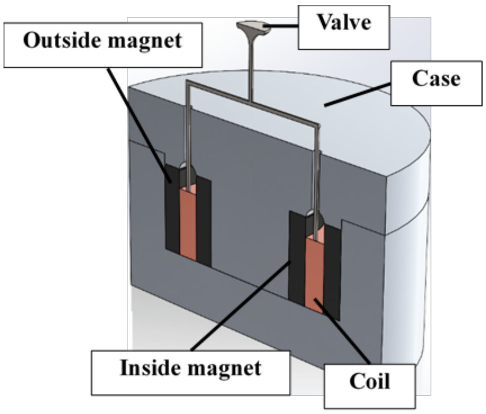

Fig. 2 Analysis model of linear actuator for EDVS.

Table 1 Materials of elements in analysis model.

Part	Measurement spot	Measurement
Case	Outer Diameter	ϕ 260 mm
	Inner Diameter	ϕ 180 mm
	Height	152 mm
	Weight	2.301 kg
Outside Magnet	Outer Diameter	ϕ 180 mm
	Inner Diameter	ϕ 148 mm
	Height	62.5 mm
Inside Magnet	Outer Diameter	ϕ 112 mm
	Inner Diameter	ϕ 80 mm
	Height	62.5 mm
Coil	Outer Diameter	ϕ 148 mm
	Inner Diameter	ϕ 112 mm
	Height	50 mm
	Turns	200 turns
Valve Head	Outer Diameter	ϕ 28 mm
	Weight	0.0366 kg

magnetic saturation and smoothen the magnetic flux flow. The case had a diameter of 260 mm and a height of 152.01 mm, which appeared very large for actual installation as part of the engine components. However, at this stage, we decided to focus on smoothing the magnetic flux flow to improve the linear motor thrust, so we selected these dimensions and shape. The materials used for each element are shown in Table 2. The case was made of permendur, which exhibits high saturation high saturation magnetic flux density, to prevent magnetic saturation. The valve was made of aluminum, which has low magnetic permeability, to prevent magnetic flux inflow. A heat-resistant samarium–cobalt magnet was added to the installed magnet.

Table 2 Material used for EDVS.

Elements	Materials
Case	YEP-2V (permendur)
Valve	Aluminum
Coil	Copper

Table 3 Analysis conditions.

Experimental conditions	Valves
Resistance	1 [Ω/m]
Voltage	20 [V]
Turn of Coil	200 turns
Mesh Size	3.5 [mm]
Number of Mesh	606593 pieces

3. Thrust Characteristics of Linear Motors Using Neodymium Permanent Magnets

3.1 *Analysis conditions*

In this study, the Lorentz force acting on the moving part of the linear motor was determined through electromagnetic field analysis using the finite element method. For the analysis conditions, a 20 A current was applied to the coil according to JSIA302 standards. The number of turns in the coil was set to 200 times. The temperatures of the model were adjusted to 20, 60, 100, and 140 °C. The mesh size was 3.5 mm, and the total number of elements in the entire model was 606593.

3.2 *Analysis results*

The thrusts obtained from the analysis were 1136 N at 20 °C and 602 N at 140 °C. The thrust decreased by approximately 50% with increasing temperature. The vector plots of the magnetic flux density of the analytical model at 20 and 140 °C are shown in Fig. 3. The magnetic flux density decreased with increasing temperature. In particular, the magnetic flux density in the coil area was 1.0 T at 20 °C and lower than 0.5 T at 140 °C. The thrust decreased as the magnetic flux flowing through the coil decreased. This decrease is attributed to a decrease in the residual magnetic flux density and coercive force caused by an increase in the temperature of the permanent magnet.

4. Thrust Characteristics of Linear Motor Using Samarium–Cobalt Permanent Magnets

4.1 *Analysis conditions*

Based on the results presented in the previous

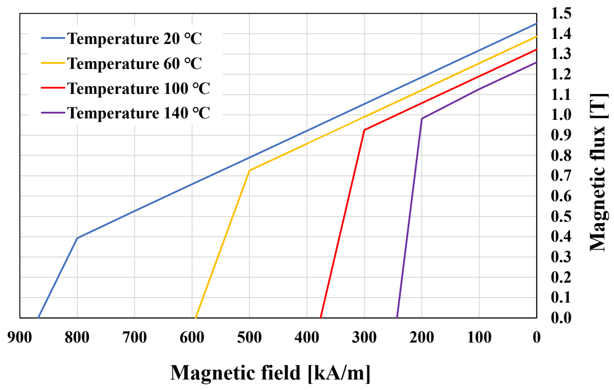

Fig. 3 B–H curves of NMX-S52[17].

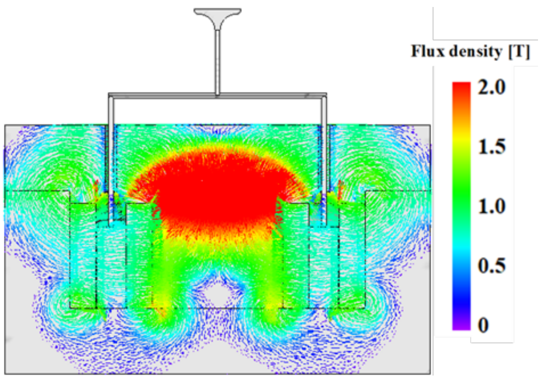

(a) 20 °C

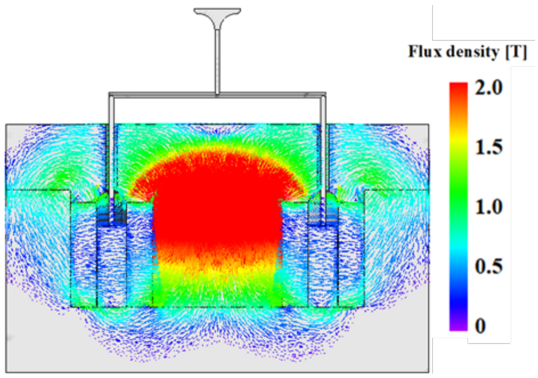

(b) 140 °C

Fig. 4 Analysis results of flux density of linear motor using neodymium permanent magnet.

section, the linear motor thrust decreased, probably owing to the thermal demagnetization of the magnet with increasing temperature. This occurred because the heat resistance of neodymium magnets was very low. Therefore, we adopted samarium–cobalt magnets, which exhibit excellent heat resistance, as the permanent magnets for the EDVS. Additionally, we investigated the thrust characteristics at high temperatures through electromagnetic field analysis using the finite element method.

A samarium–cobalt magnet, LM-32SH, was used as the permanent magnet in the analytical model. The demagnetization curves of the LM-32SH for different temperatures are shown in Fig. 5. The decrease in the residual flux density of LM-32SH with increasing temperature was approximately 0.07 T lower than the maximum value. The other analysis conditions were somewhat similar to those presented in the previous section, and the model temperatures were 20, 50, 100, 150, and 200 °C.

4.2 *Analysis results*

The thrust forces obtained from the analysis were 869 N at 20 °C and 794 N at 200 °C. The thrust force decreased by approximately 10% with increasing temperature. The vector plots of the magnetic flux density of the analytical model at 20 and 200 °C are shown in Fig. 6. Compared to the case of 20 °C, the magnetic flux density flowing through the coil did not vary significantly at 200 °C. Hence, the thrust did not decrease significantly.

The relationship between the thrust and temperature for each permanent magnet is shown in Fig. 7. The neodymium magnet with a high remanent flux density showed higher thrust than the samarium–cobalt magnet below 100 °C. The thrust of the proposed actuator at 200 °C was 794.6 N. Since the thrust required to displace the mover by 10 mm at 7000 rpm is 660.0 N, it is shown that the proposed actuator can operate over 7000 rpm even when heated to 200 °C. The thrust of the samarium–cobalt magnet did not change significantly with temperature and was maintained even above 100 °C.

5. Summary

In this study, the effect of the operating temperature on the thrust characteristics of a linear motor used in an EDVS was investigated through electromagnetic field analysis using the finite element method. From the analysis results, the thrust characteristics of the neodymium permanent magnet significantly declined at temperatures higher than 100 °C. However, those of the samarium–cobalt magnet did not change significantly even at 200°C.

The exhaust valve temperature of the engine is 600 °C or higher when used in actual equipment. Therefore, the linear motor temperature may rise to 100 °C or higher, owing to heat conduction. Although the thrust at low temperatures is low, a system suitable for several applications can be constructed using samarium–cobalt magnets, which exhibit excellent heat resistance. Neodymium magnets with high thrust should be used

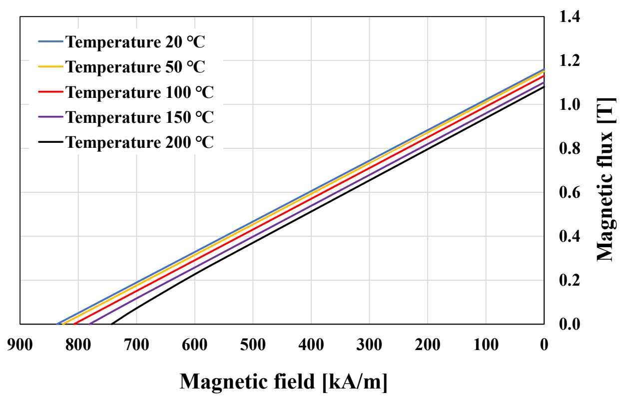

Fig. 5 B–H curves of LM-32SH[18].

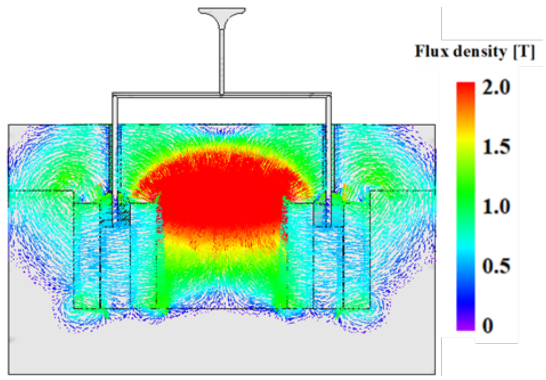

(a) 20 °C

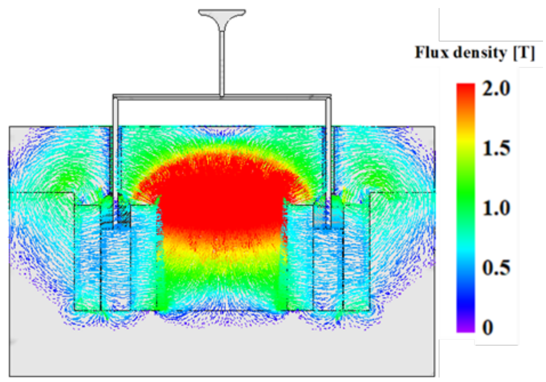

(b) 200 °C

Fig. 6 Analysis results of flux density of linear motor using samarium–cobalt permanent magnet.

under operating conditions that require higher thrust than samarium–cobalt magnets. However, the performance of neodymium magnets deteriorates, owing to thermal demagnetization. Therefore, it is necessary to design a cooling system to prevent the motor temperature from rising.

Although the size of the actuator used for installation in this study was very large, it was adopted to achieve this system by driving two intakes or exhaust valves. In the future, we will further improve the model and conduct a detailed study on the thermal distribution of

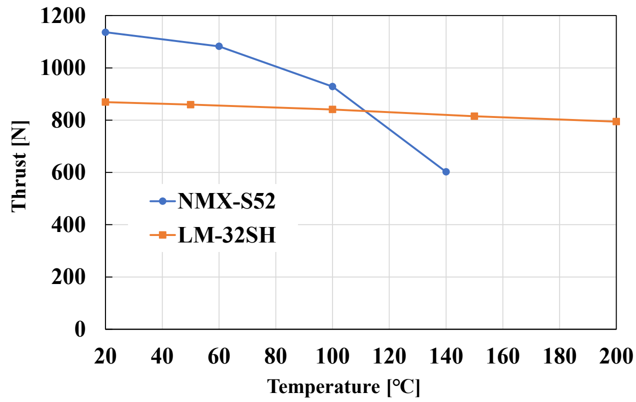

Fig. 7 Relationship between temperature of analysis model and analyzed thrust.

the EDVS and heat transfer to the magnets.

References

1) Subaru Corporation, EyeSight, Inc., https://www.subaru.jp /safety/eyesight/
2) Honda Motor Co., Ltd., Honda Sensing, A Safe Driving Support System, https://www.honda.co.jp/hondasensing/
3) Nissan Motor Corporation, ProPILOT, https://www.nissan.co.jp/BRAND/TFL/PPC/
4) All the More Reason Why Precious Metals Will Be a "Key Material" in the Automotive Industry in 2040, https://www.businessinsider.jp/post-180754
5) Y. Hayashi, Thorough Study of Racing Engines, Grand Prix BOOK PUBLISHING CO.LTD., pp. 32–57 (1992).
6) Honda Motor, Technology Zukan, https://www.honda.co.jp /tech/auto/vtec/
7) M. Uchida, H. Hasegawa, Y. Morita and T. Yabumi, Positioning Control of Electromagnetic Engine Valve using Sliding Mode Control (Improvement of control performances in valve opening period using feed forward compensation), Journal of the Japan Society of Applied Electromagnetics, Vol. 18, No. 1, pp. 48-53 (2010).
8) Y. Okada, T. Niibori, K. Matsuda and S. Hara, Development of electromagnetic valve actuator for automobile engine, Journal of the Japan Society of Applied Electromagnetics, Vol. 11, No. 1, pp. 30-36, (2003).
9) N. Tanaka, J. Iwade and Akihiko Kawada, Development of a Temperature Measurement Method for Sodium-Filled Exhaust Valves During Engine Operation, Transactions of the Society of Automotive Engineers of Japan 46, No. 2, pp. 319–324, (2015).
10) M. Uno, Y. Muraguchi, M. Konno, Y. Okada, Speed-Up Trial of Electromagnetic Engine Valve, The

Proceedings of the 10th Symposium on the Motion and Vibration Control, pp. 177-180 (2007).

11) Y. Shibasaki, A. Okazaki, M. Ogura, PWM control for Electromagnetic Valve in ICE, Proceedings of the 19th Kanto Branch Conference of the Japan Society of Mechanical Engineers, pp. 451-452 (2013).

12) Y. Sato, T. Narita and H. Kato, Valve Mechanism for Gasoline Engine with Linear Motor (Fundamental Consideration Using Electromagnetic Field Analysis), Proc. Sch. Eng. Tokai Univ., Ser. E, Vol. 44, pp. 35–39, (2019).

13) Y. Majima, T. Narita and H. Kato, A Study on High Performance of Gasoline Engine Using Linear Actuator, Proc. 60th Annual Meeting Kanto Student Association, 503, (2021).

14) T. Schroeder, R. R. Henry, and B. P. B. Lequesne, Murty, B. V, Method and Apparatus for Electrically Driving Engine Valves, U.S. Patent 5327856, (1994).

15) T. Moriya, Y. Komatsu, H. Sono and T. Sugai, Energization Control Method and Electromagnetic Control System in Electromagnetic Driving Device, U.S. Patent 5636601, (1997).

16) A. Okazaki, T. Hasegawa and Y. Nemoto, Develop of Variable Valve Actuation Gear for Automobile, Vol. 16, No. 1, pp. 29–34, (2014).

17) Nd-Fe-B Magnets NEOMAX Magnetic Property Curve, https://www.hitachimetals.co.jp/products/auto/el/pdf/nmx.pdf

18) Permanent Magnets, https://www.tokin.com/product/pdf_dl/eikyu_jisyaku.pdf